# Conceptual design of a short-pulsed net power gain experiment based on the spherical tokamak

Iliffe, William R.

*Award date:*
2017

Eindhoven University of Technology

**MASTERS THESIS**


Mr. William R Iliffe

# Conceptual Design of a short-pulsed Net Power Gain Experiment based on the Spherical Tokamak.

Fusion Department

University Supervisor: Prof. Niek Lopes Cardozo
Tokamak Energy Supervisor: Mr. Alan Sykes
Study programme: Fusion Masters

Eindhoven 2017

Title: Conceptual Design of a short-pulsed Net Power Gain Experiment based on the Spherical Tokamak.

Author: Mr. William R Iliffe

Department: Fusion Department

Supervisor: Prof. Niek Lopes Cardozo, Fusion

Abstract: Generating cost-effective electricity from the heat released from fusion reactions has the potential to revolutionize the way electricity is produced. Although much progress has been made since the 1950s in implementing such a reactor, further experimentation is still required. A review of current and proposed fusion research activities was conducted and, based on these findings, this work aims to develop a concept design for a spherical tokamak that can achieve a net power gain ($Q$) of $\geq 2.5$. Such an experiment could prove a worthwhile tool for investigating what are known as 'burning plasmas' if it can be built cost-effectively.

In order to convergence on this cost-effective Net Power Gain Experiment (NPGX), investigations were performed to assess how the cost of such a device is dependent on its components (section 2) and how the physics and engineering aspects of spherical tokamak design determine its performance (section 3). Models based on these investigations were then developed (section 4) in order to determine the most cost-effective and viable NPGX. Results imply that a spherical tokamak of major radius: $R_0 = 1.13$m and aspect ratio: $A = 1.85$ could produce fusion power: $P_{fus} = 125$MW at $Q = 2.55$ and be constructed for total project cost of £1.08bn (section 5). Recommended further work, before moving on to a more detailed design study, includes defining a more detailed cost model, defining a more rigorous approach to the design of the neutron shielding, adding complexity to the 0D description of the plasma and including an assembly procedure as part of the tokamak design.

Keywords: Fusion, Experiment, Net Power Gain, Tokamak, Spherical, Concept, Design study

# Contents

# 1. Introduction

## 1.1 World Energy Demand

During the course of this century, the energy landscape of the world will change considerably. This change is being perpetuated by a number of factors including a rising world population (predicted to reach 7.6-10.6bn by 2100 [1]), increased standards of living and the limited supply of fossil fuels [2].

Considered together, these factors have the potential to increase the world's total energy demand by over 300% by 2050 but climate change and emissions targets set by the Kyoto protocol[3] mean that the options for generating this energy are becoming increasingly limited.

Coupled with the increased electrification of transport [4], world electricity use has the potential to rise from 3.2TW (2013) to more than 21.6TW by 2050[1] [5, 6] and producing this electricity whilst remaining carbon-neutral is a big challenge for energy researchers.

## 1.2 Nuclear Fusion

One option for generating large quantities of near-carbon-neutral electricity is to use concepts based on nuclear fusion reactions. During these reactions, two light nuclei fuse to form other elemental particles, losing total mass and releasing energy. The most promising fusion reaction is that between deuterium (D) and tritium (T) as it has a higher reactivity than other potential reactions at relatively low temperatures (see figure 1.1). These two isotopes of hydrogen fuse to form helium, releasing a neutron and energy in the process:

$$D + T \rightarrow He^4(3.5\text{MeV}) + n(14.1\text{MeV}) \tag{1.1}$$

In table 1.1, the energy density of this fusion reaction is compared to other candidate energy sources. The table indicates that the energy density of DT fusion is an order of magnitude higher than uranium fission and many orders of magnitude higher than conventional chemical energy sources. As deuterium is readily available in sea water and tritium can be produced from abundant lithium, the development of a DT fusion reactor as a source of electricity has the potential to provide abundant electricity.

Efforts to implement DT fusion have come a long way since research began in the 1950s [10]. Although there are various types of fusion devices, all aim to efficiently confine reactant particles for sufficient time and with sufficient energy to overcome the coulomb repulsion between the reactant's positively charged nuclei. For DT fusion, this requires temperatures of >115,000,000K or 10keV (see figure 1.1) and at these temperatures, the reactants are in a plasma state.

Achieving and maintaining the adequate particle energies for fusion is one of the principle difficulties of initiating fusion, as the reactants quickly lose energy when they come into contact with energy sinks such as solid surfaces. Even in

[1] this is based on a averaged continuous use rate over a period of a year. For reasoning behind 21.6TW figure, see Appendix A. Data from 2013.

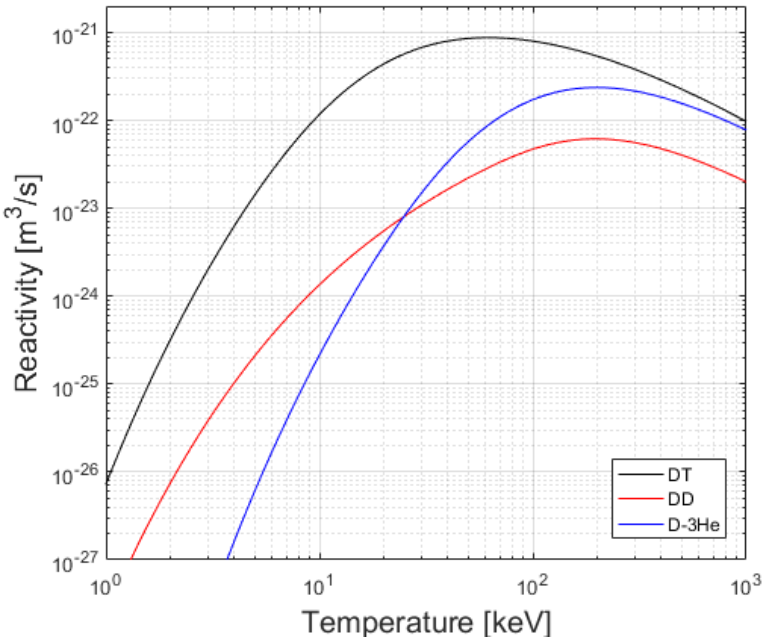


Figure 1.1: The reactivity $\langle \sigma v \rangle$ of the fusion reactions (D+D), (D+T) and (D+$^3$He) as a function of reactant temperature, drawn from data published by Li et al. [7].

the most capable fusion devices, these losses are large and considerable effort is required to maintain fusion-relevant plasma energies. In present day devices, this is achieved from external sources but, ideally for a fusion power reactor, the energy of the alpha particles resulting from fusion reactions ($P_\alpha$) would maintain the plasma's energy equilibrium.

In 1956, Lawson J.D. [11] defined the conditions of a 'ignited' DT plasma as when the alpha particle heating due to DT fusion reactions is greater than or equal to the energy losses by conduction ($P_\alpha \geq \frac{W}{\tau_e}$). For a 50-50 mixture of deuterium and tritium, this resulted in the following criterion for a ignited plasma [9]:

$$(p\,\tau_e)_I \geq \frac{24}{E_\alpha} \frac{\langle T \rangle^2}{\langle \sigma v \rangle} \tag{1.2}$$

where $W$ is the plasma thermal energy, $\tau_e$ is the characteristic timescale for energy to be lost from the plasma by conduction (known as the energy confinement time), $p$ is the plasma pressure, $\langle T \rangle$ is the volume average plasma temperature, $E_\alpha$ is the energy of the alpha particle released during DT fusion reactions and $\langle \sigma v \rangle$ is the reactivity of deuterium (D) with tritium (T) (shown in figure 1.1). $(p\,\tau_e)$ is often referred to as the 'fusion gain' of a plasma. Lawson's criterion implies that a DT plasma can become self-heating when it has sufficiently well confined energy for its combination of pressure and temperature(figure 1.2).

For present day fusion devices, external heating sources ($P_{aux}$) are required resulting in a modification to Lawson's criterion ($P_\alpha + P_{aux} \geq \frac{W}{\tau_e}$):

$$(p\,\tau_e)_Q \geq (p\,\tau_e)_I \left( \frac{Q}{Q+5} \right) \tag{1.3}$$

Table 1.1: Fuel energy density comparison. Data taken from [8] unless otherwise stated. 'Burn Rate 2050' is to produce 21.6TW of electrical power at a power plant efficiency of 40% using solely that Fuel.

| **Fuel** | **Energy Density** | **Burn Rate 2050** ($21.6TW_e$) |
|---|---|---|
| [units] | [MJ/kg] | [kg/s] |
| Wood | 16 | 3,400,000 |
| Coal | 24 | 2,200,000 |
| Diesel | 45 | 1,200,000 |
| Natural Gas | 55 | 950,000 |
| Uranium-235 | 3,900,000 | 13.8 |
| DT Fusion[9] | 30,000,000 | 0.18 |

where $Q = \frac{P_{fus}}{P_{aux}}$ is the net power gain[2]. Equation (1.3) is plotted for a $Q = 1$ and $Q = \infty$ (equivalent to $P_{aux} = 0$) in figure 1.2 and this implies that, regardless of the confinement scheme or whether external heating is used, the net power gain of a DT fusion plasma is maximized at temperatures of 13-14keV.

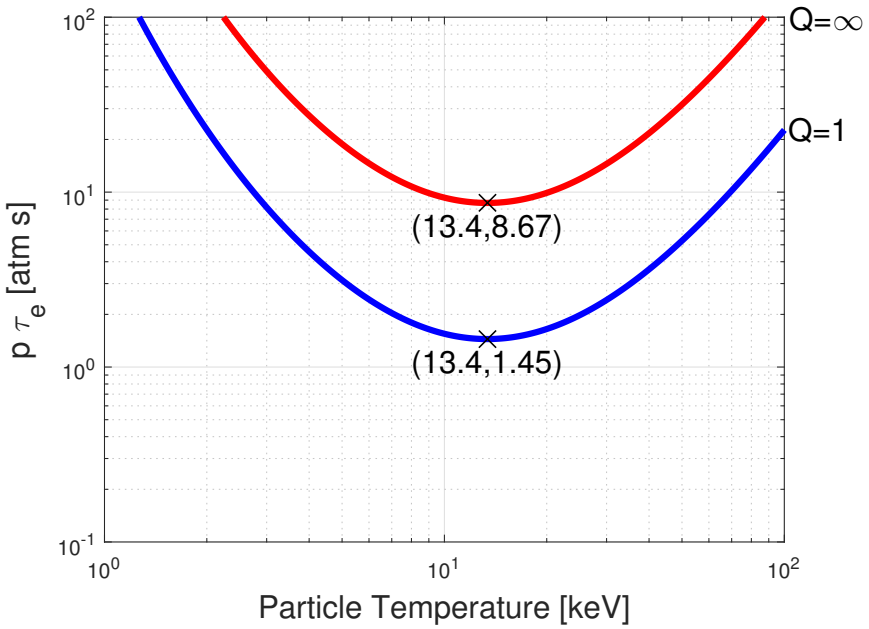


Figure 1.2: Critical $p\tau_e$ for ignition ($Q = \infty$) and Q=1 of a DT fusion plasma as a function of particle temperature calculated from equation (1.3).

## 1.3 The Tokamak

There are various ways of achieving the required combinations of plasma pressure, temperature and energy confinement for sustained DT fusion. One class of devices, known as Magnetic Confinement Fusion (MCF) devices, uses the fact

[2] $P_{fus} = P_\alpha + P_n$ where $P_n$ is the neutron power.

that at the high temperatures required for fusion, the reactants are in a plasma state. When an external magnetic field is applied to a plasma, the plasma particles, being charged, feel a Lorentz force that results in them gyrating around the magnetic field lines. This gyration has a characteristic radius which is inversely proportional to the magnetic field strength[9] and results in a decrease in the particle movement perpendicular to the field lines by over 10 orders-of-magnitude compared with along the fields when applied.

The tokamak is one such MCF device (figure 1.3). It uses a combination of toroidal and poloidal magnetic fields to stably confine a plasma away from the walls of a torus-shaped vessel[12]. This results in a pressure gradient through the plasma which peaks near its poloidal center.

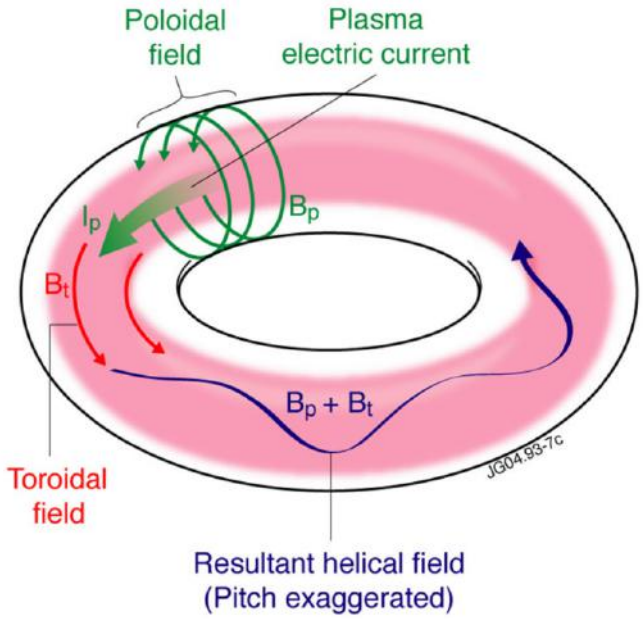


Figure 1.3: Schematic of a Tokamak Plasma (such as JET) showing direction of toroidal magnetic field($B_t$), applied by a toroidal electromagnet and the poloidal magnetic field, applied by the plasma current($I_p$)[13].

Since its inception, the tokamak has proved successful in stably confining plasma at temperatures sufficient for fusion. The largest tokamak experiment currently operating is the Joint European Torus (JET), based at the Culham Center for Fusion Energy (CCFE), UK. In 1997, this experiment achieved the current record for net power gain from a DT plasma ($Q = 0.55$)[14] and is currently preparing for more DT experiments [15].

Also based at the CCFE is the MAST tokamak. Unlike JET, MAST was built with a low aspect ratio ($A \leq 2$)[3] to take advantage of the improvements in plasma stability that offers. This improvement was first demonstrated by MAST's predecessor tokamak START when it achieved record toroidal beta[4] in 1998[16]. High beta operation is an advantage in a fusion reactor so this result led to an increase in research into how spherical tokamaks(ST) could form the basis of fusion power plants. As a result, there are now 17 operating STs worldwide

[3] $A = \frac{R_0}{a}$ where $R_0$ is the tokamak's major radius and $a$ is its minor radius

[4] ratio of plasma pressure to confining magnetic pressure due to the toroidal field

[17] and various ST-based power plants concepts have been published[18, 19, 20, 21, 22].

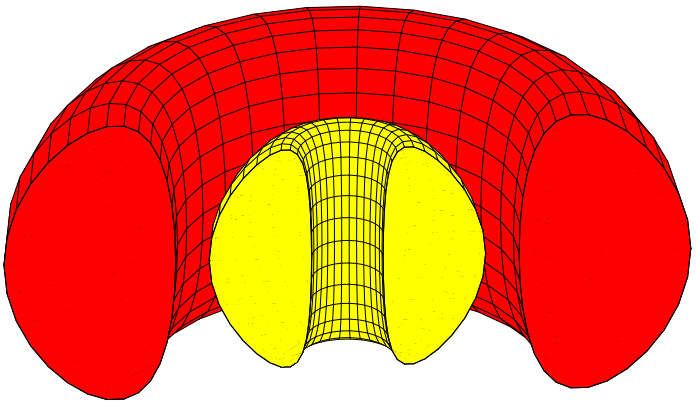

Figure 1.4: Graphic showing the difference between the typical vertically elongated shapes of plasmas in JET, which a 'conventional' aspect ratio tokamak (red), and a small aspect ratio 'spherical' tokamak of $R_0$=1m and $A$=1.7(yellow).

## 1.4 The Tokamak Routes to Fusion

Although JET is an enormously important experiment, the next stage of the development path for conventional tokamaks is not a fusion power plant but another experiment: the ITER tokamak[23]. One of the specifications of ITER is that it sustain moderate net power gain DT plasmas (Q=10 and Q=5 using non-inductive current drive) for periods of up to 400 seconds [24]. Data from ITER will be used to answer some of the open design questions about the first fusion power reactor DEMO[25].

Although the design of this DEMO reactor, and the development pathway that leads to it, is well defined [25], technological developments may offer other routes to a fusion reactor. One example of this is the SPARC/ARC route to fusion power which makes use of high temperature superconducting (HTS) materials based on REBCO[5] to access higher magnetic fields, allowing smaller, more power dense, reactors to be built [26, 27]. In both these development pathways, intermediate stepping stone reactors - ITER and SPARC - are used to resolve technological uncertainties before moving on to fusion power plants. The key difference between these routes, however, concerns their development philosophies, with the ITER project seeking to address a wide variety of physics and engineering challenges, whereas SPARC intentionally avoids goals not directly related to its primary objectives (eg. achieving Q=2-3) to save time and money.

The use of HTS is also seen as a key enabling technology in the spherical tokamak route to fusion. Tokamak Energy's ST135 concept hopes to combine

[5]REBCO is a ceramic made from a combination of rare-earth minerals (typically Yttrium or Gadolinium), barium and copper oxide

HTS with the benefits of STs to achieve a modular fusion reactor design capable of $P_{fus}$=100MW and Q=10 [28]. That said, the spherical tokamak is not as well developed as the conventional tokamak so experimentation with intermediate devices is required. Although development work is continuing on the MAST[29] and NSTX[30] STs, a new high field ST is current being built by Tokamak Energy near Oxford, UK. Designated ST40, this ST aims to achieve ($p\tau_E$)= 0.1 [atm s] at a temperature of ≈ 8.5keV, making it the most advanced ST in existence [31] but not yet close to conditions needed for DT fusion.

## 1.5 The Net Power Gain eXperiment

Based on the above, it can be reasoned that it is too soon to start the detailed design of a fusion power plant based on the combination of HTS and the ST as a number of technological uncertainties still remain. Of these uncertainties, the most potentially problematic is whether an ST can achieve the ($p\tau_E$) required for DT fusion and sustain it whilst fusion reactions heat the plasma and its components are bombarded with neutrons. This difficulty is recognized by the other development pathways which make use of intermediate level net power gain (Q=1-10) experiments. It can therefore be reasoned that a net power gain experiment (designated hereafter as the NPGX) is required in the development of STs.

Determining what level of net power gain would be an appropriate target for the NPGX requires a review of what has been achieved by current experiments and what targets have been set for future experiments. Given that no JET-equivalent ST currently exists, it can be reasoned that an ITER level net power gain is an extrapolation too far. Although, as JET has achieved a $Q = 0.55$, the NPGX should aim to exceed this target. It was therefore decided that the NPGX should aim for a $Q \geq 2.5$, similar to the SPARC concept, as this splits the difference in terms of the fraction of the plasma's alpha particle heating between what JET has achieved and what ITER aims to achieve in steady state (see figure 1.5).

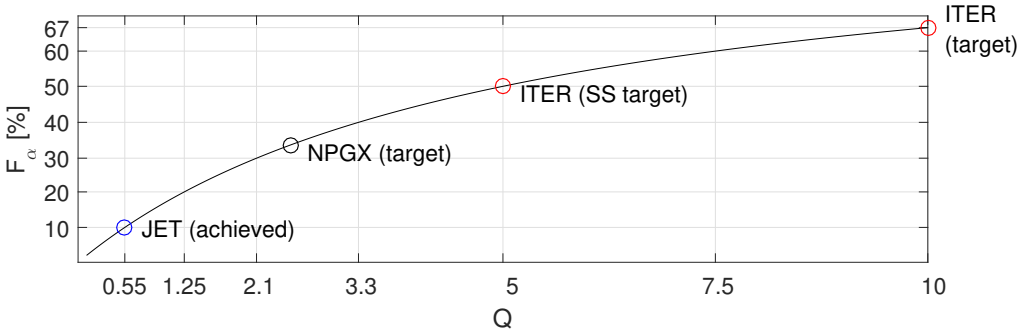


Figure 1.5: Graph showing how the fraction of the heating power provided by alpha particle heating ($F_\alpha$) varies for increasing net fusion power gain (Q). The achieved and target net power gains are marked for JET and ITER. The NPGX target power gain has been chosen as Q=2.5, equivalent to a plasma with 33.3% alpha particle heating.

Preventing the immediate implementation of this experiment, however, is the fact that present day tokamak experiments require a large initial capital investment. The estimated capital employed to build and modify the JET tokamak to get $Q = 0.55$ was roughly £1bn[29] and similar sums are expected for building the NPGX. As the degree of difficulty in raising the required funds, from either public institutions or private investment, is directly related to amounts required, the NPGX will be optimized to achieve $Q \geq 2.5$ for minimal cost. This minimal cost requirement implies that a primary-goal-only design philosophy, similar to that used for SPARC, should be followed.

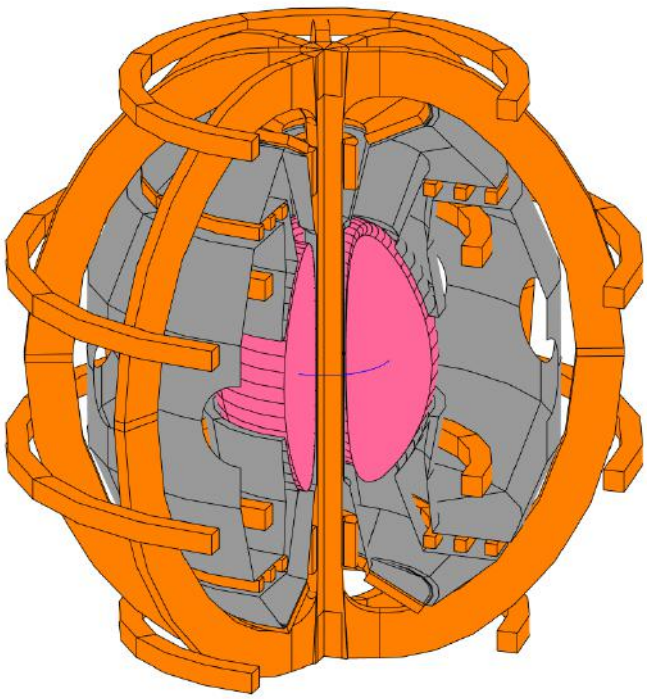

Figure 1.6: Simplistic representation of the FPD showing the plasma (purple), inner vacuum chamber (IVC) complete with attached divertor and merging compression chamber (grey) and TF, VF, PF and MC coils (orange). The NPGX design is of similar layout to the FPD.

In order to more quickly convergence on this minimal cost NPGX, it is assumed that the layout of the tokamak follows an established design provided by the project's sponsor, Tokamak Energy Ltd (TE). Although inspiration is drawn from all appropriate quarters, the starting point for the design effort is a concept known as the Fusion Power Demonstrator (FPD). Figure 1.6 shows an artists impression of the FPD showing approximate locations of coils (orange), inner vacuum vessel (grey), double-null divertor (DND) and plasma (purple). This was developed internally by TE and its consultants and draws on the company's experience at building STs to a limited budget.

The key features of the FPD are:

- Double-shell vacuum vessel for high-quality vacuum (outer vacuum chamber (OVC) not shown in figure 1.6).
- Toroidal Field coil made from Oxygen-free copper (OFCu) and consisting of a common centerpost.

- Each TF coil return limb is powered by its own super-capacitor bank.
- The TF coils are cooled by liquid nitrogen ($LN_2$) to operate in the temperature range of 80-180K. This increases the coil's performance as, in this temperature range, OFCu has a lower resistivity and higher yield stress which allows longer operation and higher magnetic fields.
- The common centerpost of the TF is to be shielded from fusion neutrons. This is primarily to prevent the neutrons heating the centerpost, allowing the TF to operate for longer.
- Merging Compression (MC) is used for plasma initiation and current ramp up. In most tokamak experiments, a central solenoid (CS), positioned about the tokamak's radial center, uses a flux swing for these purposes and then to maintain the plasma current. Importantly, it is the size of the total flux swing that defines the CS's physical size but a large proportion of the CS's flux swing is consumed by these initial stages. By initiating the plasma with MC instead, the CS can be greatly reduced in size or even eliminated. Although the use of MC requires an overall increase in the size of the tokamak, it is advantageous in STs as it moves the volume requirement from the tokamak's radial center, which is also needed by the centerpost, to the outside of the plasma. (MC is described in more detail in section 3.2.5).
- Based on the above, there is currently no plans to include an CS in the NPGX design. Therefore the MC system should be designed to achieve the required plasma current before non-inductive or solenoid-free inductive current drive is used to maintain the plasma current.
- Neutral Beam Injection (NBI) is used for non-inductive current drive and plasma heating.

The implications resulting from these design choices are expanded upon in later sections.

Based on the above, the research question for this work is defined as:

> What capital expenditure is required to build a Spherical Tokamak experiment based on TE's "Fusion Power Demonstrator" concept that can sustain a $Q \geq 2.5$?

## 1.6 Methodology

Assessing the capabilities and costs associated with an ST experiment requires the design to be assessed from multiple viewpoints. For this work, these viewpoints are limited to the associated plasma physics, mechanical & electrical engineering and cost factors. The parameter space for ST comparison are defined as:

- Major Radii: $0.6 < R_0 < 1.5$m. The lower bound of $R_0$ is set by the size of TE's proposed HTS demonstrator tokamak ST60[31] and the upper bound was chosen so it slightly exceeded that of TE's fusion power plant concept ST135 [22, 31].

- Aspect Ratio: $1.4 < A < 2$. This range accounts for the minimum aspect ratio achievable by current STs[32] and goes slightly beyond the typical aspect ratios chosen for ST-based fusion reactors[20, 22, 33].

The project's work flow consists of a three stage investigation. The first consists of a literature search concerning the costs associated with tokamak experiments. This is used to determine which of the NPGX components constitute good proxies for larger system costs and how these costs scale with component properties. The desired result is a cost model capable of estimating the price of each candidate tokamak.

The second stage considers, from a theoretical standpoint, the relevant physics and engineering factors associated with ST design in order to establish inputs for the cost model. As briefly eluded to above, a great deal of work has been done by others on the conceptual design of fusion experiments and reactors. The literature describing these works and how they were defined are studied and used to:

1. Reduce the number of independent variables associated with tokamaks by either determining realistic values that can be assumed constant throughout the analysis or making them functions of other independent variables.

2. Determine methods of estimating the inputs to the cost model that take the relevant physics and engineering into account.

Finally, an optimization that can identify the NPGX design that achieves the required net power gain at minimal cost is performed. This is achieved by using computer models to investigate the physics and engineering aspects of each considered NPGX design. The physics modeling is done in conjunction with the thesis project's sponsor Tokamak Energy Ltd (TE) and is implemented in MATLAB [34] as provided by Eindhoven University of Technology (TU/e). The mechanical engineering modeling of the relevant mechanical components is completed using the COMSOL finite element analysis tool [35] as provided by TU/e. Relevant information from all of these modeling steps is then fed back into the cost model, allowing the capital cost of each candidate ST to be calculated and compared.

# 2. Cost Investigation

To build a cost model for the NPGX, a list of the required components is needed. The list that forms the basis of this cost model was published by ITER organization as part of the ITER Engineering Design Activities in 1999[36]. This list has been analysed with regard to the requirements of the NPGX and the cost data from 2 tokamaks (ITER[36, 38, 39] and TE's ST40[1]). The outcome of this analysis is summarized in table 2.1. Due to the similarities between the NPGX's tokamak core and the ST40 design, data from ST40 is used as a cost basis for the tokamak core with the exception of the blanket. Regarding the auxiliary systems, a mixture of cost bases are required.

In the analysis of J. Freidberg [9], it is assumed that the cost of each tokamak component is proportional to its volume. This indicates that some volumetric or quantity-based indicator can be used as a reasonable proxy between the size and cost of each component. In this section, a suitable number of proxies to use as a basis for the cost of the NPGX is determined.

Where cost estimates are stated in currencies other that GBP and at dates different to that established as a basis for this project (December 2016), the values are converted first to GBP at the date of the estimate[40] and inflated to December 2016 values[41].

## 2.1 ST40 data derived Costs

In this section, data about the costs incurred by the TE's ST40 tokamak are presented in order to determine a cost basis for the tokamak's machine core, cooling systems, power supplies, Diagnostics and Control, Data Acquisition and Communication (CODAC) system.

ST40 is being built in a number of phases, each of which needs to achieve a predefined set of physics and engineering goals before moving on to the next phase. Each of these phases incurs extra costs for upgrades and ST40 will be operating at rated toroidal field ($B_0$: 3T) and with NBI heating at the end of phase 3. The capital costs incurred up to phase 3 can be split into 3 broad groups: building and assembling the tokamak, building and commissioning the power supplies and installing the plasma heating systems. A breakdown of the proportions of each of these cost for TE's ST40 is shown in figure 2.1. The cost of the power supplies and tokamak are summarized in figure 2.2.

Figure 2.2 (left) indicates that the largest proportion (21%) of the tokamak core cost, including CODAC, Diagnostics and liquid nitrogen cooling system, is the TF coil. If it is assumed that these costs scale linearly with plasma volume, it can be reasoned that estimating the TF coil cost can give an indication of the total cost of all these components. As ST40's TF coils are made from the same material as the NPGX's coils, the volume of OFCu that made up part of the finished TF coil ($V_{OFCu}^{[m^3]}$) was chosen as the volumetric cost indicator. Based on data provided by TE, the cost of an OFCu TF coil per cubic meter was approximately $1.1[M£/m^3]$.

[1] All data concerning TE's ST40 is sourced from Tokamak Energy Ltd internal documentation and that TE asked that only relative cost information be presented.

Table 2.1: Cost basis analysis for the NGPX based on required list of ITER components from [36]

| | | **Required by...** | | | |
|---|---|---|---|---|---|
| | | **ITER** | **ST40** | **NPGX** | **Chosen Cost Basis** |
| **Machine Core** | Magnet Systems | Y | Y | Y | ST40 |
| | Vacuum Vessel | Y | Y | Y | ST40 |
| | Blanket System | Y | | Y | ITER |
| | Divertor | Y | Y | Y | ST40 |
| | Machine Assembly | Y | Y | Y | ST40 |
| | Cryostat | Y | | | |
| | Thermal Shields | Y | Y | Y | ST40 |
| | Vacuum Pumping & Fueling System | Y | Y | Y | ST40 |
| **Auxiliares** | Remote Handling Equipment | Y | | Y | ITER |
| | Cooling Water Systems | Y | Y | (1) | ST40 |
| | Tritium Plant | Y | Y | Y | ITER |
| | Cryoplant & distribution | Y | (2) | (2) | ST40 |
| | Power Supplies & Distribution | Y | Y | Y | ST40 |
| | Buildings | Y | | (3) | (4) |
| | Waste Treatment and Storage | Y | Y | Y | ITER |
| | Radiological Protection | Y | | Y | ITER |
| **H&CD** | Ion Cyclotron | Y | | | |
| | Electron Cyclotron | Y | | | |
| | NBI | Y | Y | Y | (5) |
| **Other** | Diagnostics | Y | Y | Y | ST40 |
| | CODAC | Y | Y | Y | ST40 |

1) NPGX will be exclusively Liquid Nitrogen Cooled
2) NPGX will only need a LN2 storage and delivery system
3) Necessary but avoidable dependent on NPGX footprint
4) ITER data unreliable. Using ARIES system code formula [37]
5) In case of Positive NBI - ST40, for Negative NBI - ITER

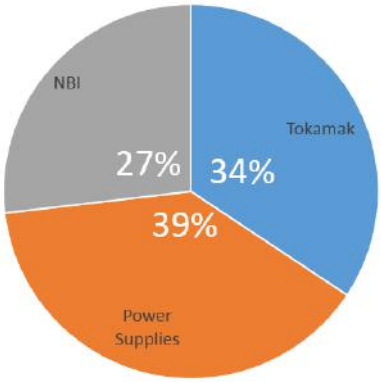


Figure 2.1: Cost estimate overview of ST40 tokamak after phase 3 ($B_0$: 3T, NBI installed).

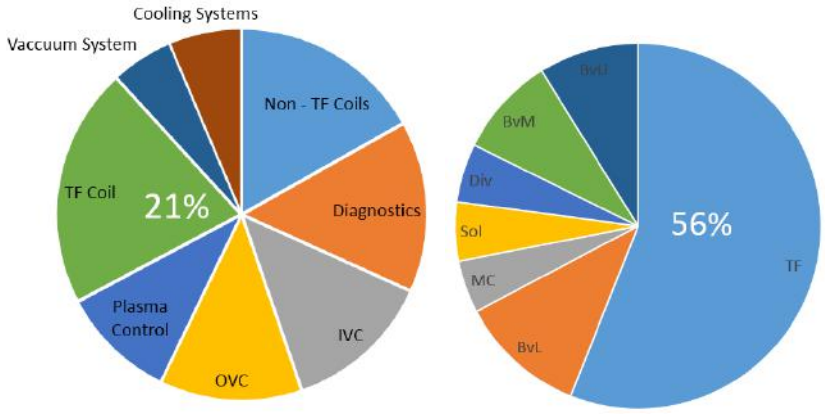


Figure 2.2: ST40 Costs: Detailed Tokamak (left) and Power Supplies (right) after phase 3 ($B_0$: 3T, NBI installed). Acronyms are (LEFT) IVC - Inner Vacuum Chamber; OVC - Outer Vacuum Chamber; (RIGHT) BvL/BvM/BvU - Lower/Middle/Upper Vertical Field Coil; MC - Merging Compression System; Sol - Central Solenoid System; Div - Divertor Coil.

On both the NPGX and ST40, the current to all coils is provided by discharging super capacitor banks. Using this method allows large currents to be provided over short periods of time. Figure 2.2 (right) indicates that the bulk (56%) of ST40's power supply cost is due to the requirements of the TF coils. In turn, the largest single item by cost for the TF coil power supply is for the purchase of super-capacitors (27.3%). It is therefore assumed that an estimate of the total number of super-capacitors to power all the NPGX's coils can be made if the number of super-capacitors required to power the TF coil is known ($N_{SC}$). Coupled with a set unit cost per super-capacitor, the total cost for all the NPGX's power supplies can be calculated. Based on advice from the project sponsor, the super-capacitor chosen as the basis for the NPGX's power supplies is the Maxwell BMOD0165 P048 BXX which can be purchased for £1200 each.

## 2.2 ITER data derived Costs

In this section, data about the costs incurred by the ITER tokamak is analysed in order to determine a cost basis for the Remote Handling Equipment, Tritium Plant, Buildings, Blanket System, Waste Treatment and Radiological Protection systems required for the NPGX.

Waste Treatment and Radiological Protection is a small percentage ($\approx 0.1\%$) of the ITER construction budget[36] and it is therefore assumed that this will be of negligible cost to the NPGX

Although this cost may be avoidable if suitable premises become available, the cost of constructing buildings to house the NPGX is likely to constitute a substantial proportion of the total cost. Based on [38, 39], the cost of ITER buildings has risen since its initial estimate in 2001 and up-to-date cost data was not publicly available. The cost of the NPGX's reactor building ($c_{rb}$) is therefore estimated based on an expression adapted from Dragojlovic et al. [37]:

$$c_{rb}[M\$1992] = 78.09\left(\frac{V_{rb}}{80000}\right)^{0.62} \tag{2.1}$$

$$V_{rb} = (6\ H_{OVC})\ \pi\ (R_{OVC}+9)^2 + 1.55\times 10^5 \tag{2.2}$$

where $V_{rb}$ is the reactor building volume and $H_{OVC}$ and $R_{OVC}$ are the height and radius of the outer vacuum vessel respectively. The cost of the reactor building can be fixed if it is designed around the largest tokamak in this project's range ($R_0 = 1.5$m) and it is assumed that: $H_{OVC} = R_{OVC} = 10R_0$. The resultant fixed cost of the reactor building is therefore assumed to be £$206m$ [2]. Dragojlovic et al. [37] also allow a cost of \$133.63m (1992) for 'Miscellaneous Buildings'. Assuming these buildings are required by the NPGX, this is equivalent to requiring an extra £463m.

Infrastructure for the safe handling of tritium are also required by the NPGX. Tritium infrastructure has a number of associated fixed costs including the handling of tritium deliveries, extraction of decay products, delivery to/from experiment, plasma exhaust processing and tritium storage[42]. It is therefore assumed that the cost of the NPGX's tritium infrastructure will be equivalent to that of ITER. Based on [36], the tritium infrastructure for ITER was estimated to cost 36.6kIUA. Accounting for exchange rates and inflation, 1IUA = £1481.7 (2016)[3] and this would make the cost of the NPGX's tritium infrastructure: £54.2m

The amount of tritium needed to run experiments could also be a significant cost. This cost contribution is based on what was required during JET's DTE1 campaign[14]. During DTE1, JET had 100g of tritium on site [43]. At \$30,000/gT [44] (2013), this represents a cost of £2.1m [4]. If the need for tritium is extended to similar levels as JET's scheduled DTE2 experiment, the expenditure on tritium would increase 5-10x [43].

Next, the blanket system is considered. Based on [36], the ITER blanket system costs 165.2kIUA, equivalent to £244.7m. As the blanket forms a shell of near-constant thickness around the plasma, it is assumed that the cost of the

[2] \$-£(1992): 1.76; GBP inflation: 97%.

[3] 1IUA=875.8ECU (1989); In 1989: 1ECU=£0.702; GBP Inflation: 242%.

[4] \$-£(2013): 1.57; GBP inflation: 8%.

ITER blanket scales with the plasma surface area. The surface area of an ITER plasma is 680m$^2$ [45], hence the blanket cost $\approx$ £360k per m$^2$. On the NPGX, the blanket only required to protect the centerpost adjacent to the plasma. This surface area ($S_c$) is:

$$S_c \approx 2\pi(R_0 - a)\kappa a \tag{2.3}$$

Assuming $\kappa = 3$, for the largest centerpost diameter is the range of STs being considered ($R_0 = 1.5$,$A = 2$), $S_c = 10.6\text{m}^2$, implying a blanket cost of £3.8m.

Finally, the cost of Remote Handling equipment (RHE) is considered. The cost for ITER's RHE is 61.1kIUA [36] which is equivalent to £90.5m. Assuming that the cost of the RHE equipment scales with the plasma volume, RHE costs can be assumed £108k per $m^3$. The largest plasma volume considered in this work is $\approx 90m^3$ so an RHE budget of $\approx$£10m is assumed.

## 2.3 Neutral Beam Heating Costs

In this section, the cost incurred for a Neutral Beam Injection (NBI) heating system is considered. In figure 2.1, the capital cost contribution for ST40's positive neutral beam (PNBI) system is calculated using the figure-of-merit: £3 per watt of power absorbed by plasma (£3/W).

In a neutral beam injector, beam particles are ionized and accelerated to high energy before being neutralized. This last stage is essential as it allows the fast beam particles to penetrate the plasma without being deflected by the tokamak's magnetic field. Once inside the plasma, the neutral particles ionize and transfer their energy to the plasma. The location at which the beam particles ionize is dependent on the plasma density and the initial beam energy. Dependent of the whether the NBI system is being used to drive current, the beam can either be oriented perpendicular to the plasma surface (heating only) or tangentially (heating and current drive). In either situation, the beam particles should have adequate energy for a sufficient fraction of particles to penetrate to the plasma center. As tangential beams have to travel further to reach the plasma center, they often require higher energy beam particles.

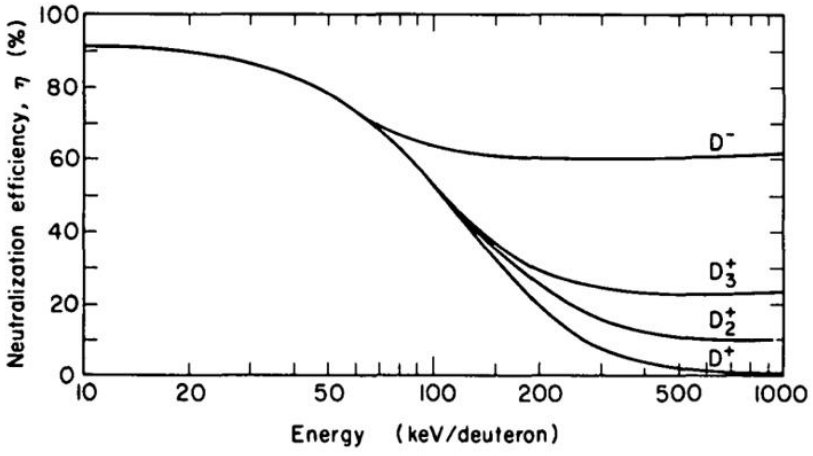


Figure 2.3: NBI Neutralizer efficiency as a function of Beam Energy [46].

Although deuterium-based PNBI systems have been used successfully on JET[47], there is a limit to the beam energy at which they can operate efficiently (see figure 2.3). Above 130 keV/D initial beam energy, the peak neutralization efficiency of positive beam ions drops to below 40% [46] and the use of Negative-ion based neutral beam injection systems (NNBI) is recommended. There is a significant chance that, like ITER[45], the NPGX will require an NNBI system. ITER's NNBI system will be capable of accelerating deuterium particles to energies of 1MeV/D and is currently being developed at the PRIMA facility in Italy [48]. Based on [36], ITER's 33MW of 1MeV NNBI should cost 96kIUA, equivalent to £142.2m (£4.3/W).

## 2.4 Cost Model Summary

By looking at the ST40-derived cost data, the following expression have been derived for the cost of the NPGX's tokamak core ($£_{tok}$) and its power supplies ($£_{ps}$):

$$£_{tok} = \frac{V_{OFCu[m^3]} \times 1.1\ [M£/m^3]}{0.210} \tag{2.4}$$

$$£_{ps} = \frac{N_{SC} \times 1200\ [£/SC]}{0.560 \times 0.273} \tag{2.5}$$

The ITER-derived cost data implies that there is a fixed cost of £669m associated with the construction of buildings to house the experiment ($£_b$) and £70.1m for the auxiliary systems($£_i$). From data concerning the provision of neutral beam heating, PNBI can be provided for £3/W and NNBI can be provided for £4.3/W

$$£_{PNBI} = 3.0[£/P_{PNBI}] \times P_{PNBI[W]} \tag{2.6}$$

$$£_{NNBI} = 4.3[£/P_{NNBI}] \times P_{NNBI[W]} \tag{2.7}$$

The cost of the NPGX device ($£_{NGPX}$) is thus defined:

$$£_{NGPX} = £_{tok} + £_{ps} + £_{PNBI} + £_{NNBI} \tag{2.8}$$

and the total cost of the project:

$$£_{TOTAL} = £_{NGPX} + £_{fix} \tag{2.9}$$

where $£_{fix} = £_b + £_i$=£739.1m.

# 3. Physical Investigation

In previous section, it was shown that the cost of the NPGX can be estimated from 4 volumetric indicators ($V_{OFCu}$, $N_{SC}$, $P_{PNBI}$, $P_{NNBI}$). In order to quantify these cost indicators, a general look at the design of STs is required. The physics knowledge relevant to the design of tokamaks is presented in section 3.1. The relevant theoretical aspects of the mechanical and electrical engineering design of the NPGX are introduced in section 3.2.

## 3.1 Physics Investigation

In this section, the physics knowledge relevant to the design of tokamaks is presented. This physics knowledge has been assembled from a number of sources but draws heavily from a number of tokamak design algorithms(TDA) and their associated references. These algorithms vary greatly in their complexity and underlying assumptions, but all seek to optimize a tokamak's physics and engineering design with respect to a figure-of-merit. The TDAs considered are PROCESS [49], HELIOS [50], the ARIES system code [37] and the Tokamak Energy System Code (TESC) [51].

### 3.1.1 Power Balance

One approach to studying fusion plasma is to consider them a mixture of species of charged particles (multiple ions species and electrons) whose physical behavior can be described by the equations of conservation of mass, energy and momentum for each plasma species. Together these form a set of coupled, non-linear partial differential equations that constitute a full 3D description of a fusion plasma. This full description of the plasma is complex and time-consuming to solve so a number of assumptions[1] can be made to reduce the system's complexity without losing a realistic representation of the bulk plasma's behavior. The outcome of applying these assumptions to the plasma's energy equilibrium is known as the 0D power balance equation and it is used by all the considered TDAs to represent the energy equilibrium of fusion plasma:

$$\frac{d\langle W\rangle}{dt} = \sum\langle S\rangle - \frac{\langle W\rangle}{\tau_e} \qquad \left[\frac{J}{m^3 s}\right] \tag{3.1}$$

where $W$ is the plasma's thermal energy, $S$ represents the sources and sinks of plasma energy and $\tau_e$ is the characteristic time scale on which energy is lost from the plasma by conduction or the 'energy confinement time'. The use of $\langle ... \rangle$ implies that that quantity is averaged over the plasma volume.

There are a number of energy sources and sinks that apply to a fusion plasma. If it is assumed that $\sum\langle S\rangle$ consists of only alpha particle and external heating, the result is equation (1.3) in section 1.2. Most of the considered TDAs use a more complete list of energy sources and sinks such that:

$$\sum S \Rightarrow f_\alpha S_\alpha + S_\Omega + S_{aux} - S_{brems} - S_{line} - S_{cyclo} \tag{3.2}$$

[1] for example, assuming the plasma is close to thermodynamic equilibrium

where $S_\alpha$, $S_\Omega$ and $S_{aux}$ represents the energy gained by the plasma due to alpha particle heating, inductive heating by the plasma current and external heating applied to the plasma respectively, $f_\alpha$ is the fraction of alpha particle energy that is absorbed by the bulk plasma before the alpha particle is lost. $S_{brems}$, $S_{line}$ and $S_{cyclo}$ represent to energy lost from the plasma due to bremsstrahlung radiation, line radiation and cyclotron emission respectively.

The degree of complexity of the mathematical expressions that estimate the magnitude of each of these terms varies between TDAs although they all involve the volume-averaging of the sources/sinks over the plasma assuming a fixed plasma boundary and simplified density and temperature profile (see section 3.1.3). (For a summary of the equations used for this work, see Appendix B.)

### 3.1.2 Use of Empirical Scaling Laws

As plasmas are very efficient conductors of thermal energy, the rate at which energy is lost from the plasma by conduction can be very large. As such, it is important for tokamaks to have good energy confinement perpendicular to the magnetic field lines. This loss rate is characterized by energy confinement time ($\tau_E$) and therefore it is important that $\tau_E$ is accurately calculated. As $\tau_E$ is a 0D representation of a complex process that is difficult to predict from first principles, all the considered TDAs estimate $\tau_E$ using empirical scaling laws whose definition is based on the regression analysis of experimental data. To maximize $\tau_E$, most of the TDAs assume operation in ELMy H-mode (discussed further in section 3.1.8) with some degree of energy confinement enhancement ($H_f$) although some TDAs offer scaling laws based on other modes of operations.

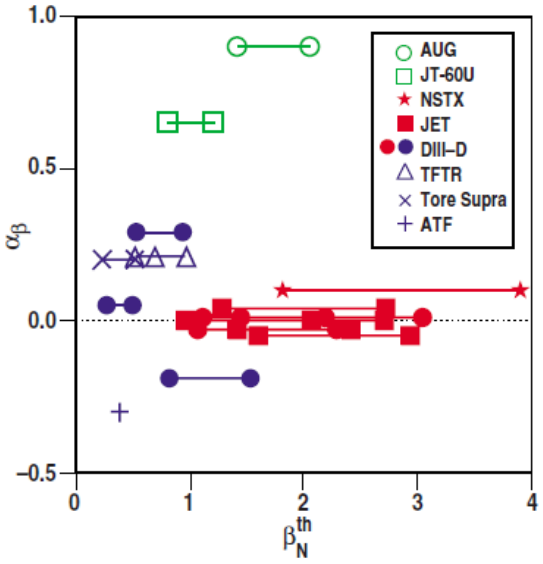


Figure 3.1: Beta Scaling exponents ($\alpha_\beta$) for the thermal energy confinement time for L-mode (blue) and H-mode (red, green) tokamak plasma measured over a range of $\beta_N$ on a variety of tokamaks (From Petty C.C. et al. [52])

The database used to define the various ELMy H-mode scaling laws has been built up over the last 30 years and contains data from a wide range of

experiments[53]. Multiple attempts have been made to analyze this data based on different assumptions and this has resulted in a number of scaling laws. One key area of debate in the literature is how energy confinement varies with the the tokamak's ratio of plasma pressure to magnetic pressure '$\beta$'. For example, the ITER98(y,2) scaling[45] has a strong negative dependence on $\beta$ whereas the PETTY08 scaling[52] is beta-independent. This is of particular importance to the NPGX as one of the advantages of STs is their ability to operate stably at high plasma $\beta$[54]. This discrepancy has resulted in two STs (MAST[55] and NSTX[56]) developing there own scaling laws based on ST data only. These scaling laws are based on the equation:

$$\tau_{E,scaling} = C \times H_f \; I_{P[MA]}^{\alpha_{I_p}} \; B_{0[T]}^{\alpha_{B_0}} \; {n_{e,20}^{-}}^{\alpha_{n_e}} \; \kappa^{\alpha_\kappa} \; A^{\alpha_A} \; R_{0[m]}^{\alpha_{R_0}} \; P_{M[MW]}^{\alpha_{P_M}} \; A_{eff}^{\alpha_{A_{eff}}} \qquad (3.3)$$

where $C$ is a constant, $I_p$ is the plasma current, $B_0$ is the toroidal magnetic field at the major radius, $\bar{n_e}$ is the line averaged electron density of the plasma, $\kappa$ is the ratio of the plasma torus's height to width (see section 3.1.3), $A$ is the plasma's aspect ratio, $P_M = (f_\alpha S_\alpha + S_\Omega + S_{aux})V_p$ is the total plasma power gain and $A_{eff}$ is the effective mass of the plasma.

The exponents for each scaling law are shown in table 3.1. These indicate that the ST-based scalings have a stronger dependence in toroidal field strength ($\alpha_{B_0}$) and weaker dependence on poloidal field strength ($\alpha_{I_p}$) than the ITPA scalings. That said, it should be noted that the databases used to define the ST-based scalings are machine-specific, contain far fewer data points ($\approx$100 compared to >10,000 for the ITPA database scalings) and use fewer variables, hence they intentionally make use of the same $\kappa$, A and $R_0$ dependence as the ITER98y2 scaling. Although this implies that the ITPA based scalings be more accurate, it should also be noted that only low $\beta$ plasmas are included in the ITPA database, limiting there applicability to the high $\beta$ plasmas available to STs.

A further complication with respect to scaling laws is in the application of energy confinement enhancement ($H_f$) as a great number of tokamak design aspects that could not easily be included in the scaling laws have an affect on energy confinement. In this regard, one key area of interest is in the use of specialized plasma facing surfaces, such as liquid lithium. The benefits of using lithium plasma facing surfaces in fusion devices have been theoretical demonstrated [57] and the technology is currently being developed [58]. Until a suitable system has been demonstrated, however, this technology will not be implemented on the NPGX. Instead, the NPGX should utilize a lithium coating on its first wall, similar to that used in the TFTR supershots [59], as this has been shown to increase the energy confinement characteristics of a tokamak [60, 61].

### 3.1.3 Definition of the Plasma Boundary

One similarity between the TDAs is that they all pay close attention to accurately replicating the shape of the plasma boundary. For simplicity, they all assume that the plasma is axisymmetric about the tokamak's central axis. Definition of the plasma boundary therefore requires a definition of the edge of the plasma's poloidal cross section. As tokamaks rely for their improved energy confinement on their magnetic field lines reconnecting after a number of turns around the torus, the edge of the plasma is therefore marked by the outermost set of magnetic field

Table 3.1: Co-efficients for the four Scaling Laws used in the project

| Scaling | C | $\alpha_{I_p}$ | $\alpha_{B_0}$ | $\alpha_{n_e}$ | $\alpha_\kappa$ | $\alpha_A$ | $\alpha_{R_0}$ | $\alpha_{P_M}$ | $\alpha_{A_{eff}}$ |
|---|---|---|---|---|---|---|---|---|---|
| | ITPA Database Based on ELMy H-mode | | | | | | | | |
| ITER98y2 [24] | 0.1445 | 0.93 | 0.15 | 0.41 | 0.78 | -0.58 | 1.97 | -0.69 | 0.19 |
| PETTY08 [52] | 0.1086 | 0.75 | 0.30 | 0.32 | 0.88 | -0.84 | 2.09 | -0.47 | 0.00 |
| | ST based | | | | | | | | |
| MAST [55] | 0.252 | 0.59 | 1.4 | 0.00 | 0.78 | -0.58 | 1.97 | -0.73 | 0.00 |
| NSTX [56] | 0.262 | 0.57 | 1.08 | 0.44 | 0.78 | -0.58 | 1.97 | -0.73 | 0.00 |

lines that reconnect without impinging on a solid surface. This poloidal surface is known as the last closed flux surface (LCFS) and its exact location depends on the magnetic topology of the tokamak.

The level of mathematical complexity used to define the shape of the LCFS varies greatly between TDAs but, once defined, the resulting expressions can be used to determine formulae for the plasma's volume and surface area. All TDAs assume LCFS shapes that are elongated ($\kappa$) and have some triangularity ($\delta$) as this allows access to higher plasma pressures due to their effects on minimizing kink instabilities (see section 3.1.6) [62]. Practicalities surrounding the design of the divertor tend to limit $\delta \leq 0.5$. Most of the considered TDAs limit plasma elongation as function of aspect ratio.

Examination of data from the ITER ELMy H-mode database [53] and Gates et al. [63] suggests the practical limit (figure 3.2):

$$\kappa_{MAX} = 3.2/A^{0.5} \tag{3.4}$$

The simplest LCFS definition in the considered TDAs is that used by the TESC code. It assumes that the LCFS shape is up-down symmetric and can be defined by two intersecting ellipses. This results in an LCFS that is defined as follows $(0 < \theta < 2\pi)$ [64]:

$$R_{LCFS}(R_0, A, \kappa, \delta) = R_0 + \frac{R_0}{A}\cos(\theta + \delta\sin(\theta)) \tag{3.5}$$

$$Z_{LCFS}(R_0, A, \kappa, \delta) = \kappa\frac{R_0}{A}\sin\theta \tag{3.6}$$

These formulae result in an LCFS shape that is a reasonably accurate approximation to those produced by MHD equilibrium solvers. An example is shown in figure 3.3. The resulting approximate expressions for the plasma surface area and volume are [51]:

$$S_p = \left[4\pi^2 A\kappa^{0.65} - 4\kappa\delta\right]a^2 \tag{3.7}$$

$$V_p = \left[2\pi^2\kappa(A-\delta) + \frac{16}{3}\pi\kappa\delta\right]a^3 \tag{3.8}$$

### 3.1.4 Volume Averaging

As described in section 3.1.1, volume averaging plasma quantities is a key step in reducing the complexity associated with assessing a tokamak plasma's ability

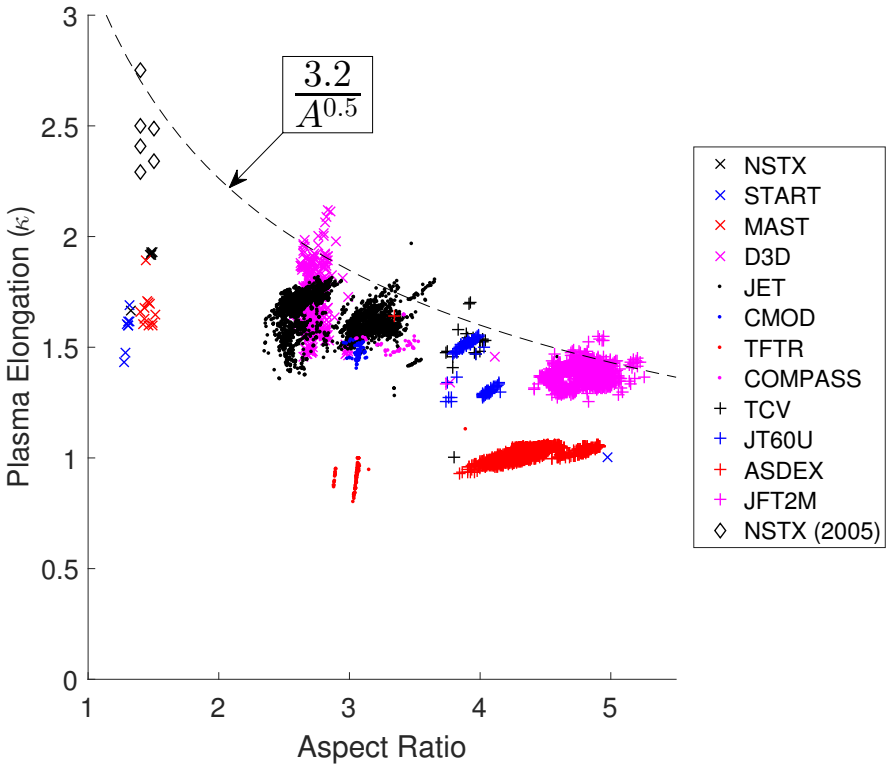


Figure 3.2: Plot of data of plasma elongation ($\kappa$) vs Aspect Ratio ($A$) from the ITER ELMy H-mode database [53]. No data filtering has been used apart from by Machine. Due to the small amount of low aspect ratio data in the database, results achieved on NSTX up to 2005 have been included[63]. Maximum achieved plasma elongations by machine suggest a maximum achievable plasma elongation of $\kappa_{Max} = 3.2/A^{0.5}$.

to sustain fusion reactions. The density and temperature in a tokamak plasma varies in three dimensions due to turbulence but, for simplicity, the considered TDAs use a 1D approximation for their profiles for volume averaging. These tend to be based on the plasma parameter peaking at the plasma's geometric major radius($R_0$) and diminishing towards the LCFS as a function of the plasma's minor radius normalized to the distance from the plasma center to the LCFS at the mid-plane ($\rho = \frac{r}{a}$). Many try to mimic, as close as possible, the radial profiles found in a realistic tokamak plasma leading to a variety of complex expressions. The simplest among the considered TDAs takes the following form [51]:

$$\Phi(\rho) = \Phi_0(1-\rho^2)^{s_\Phi} \qquad 0 < \rho < 1 \tag{3.9}$$

where '$\Phi$' is the variable being considered (typically number density(n), temperature (T) or current density (j)), the subscript '0' denotes the value of $\Phi$ at the tokamak's major radius ($R_0$) and $s_\Phi$ is the profile shaping factor.

This allows the plasma parameters measured at $(R_0, 0)$ to be related to the volume averaged value by the equality:

$$\Phi_0 = \langle\Phi\rangle(1+s_\Phi) \tag{3.10}$$

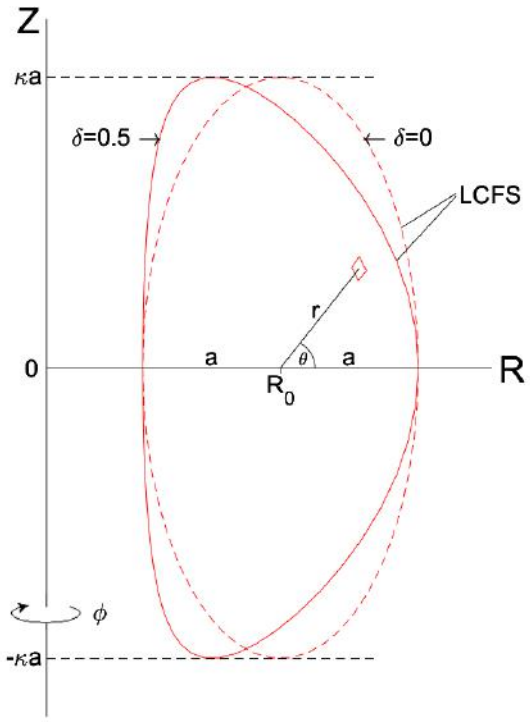


Figure 3.3: Description of the Poloidal Section as defined by $(R_0, A, \kappa, \delta)$ used to define the NPGX.

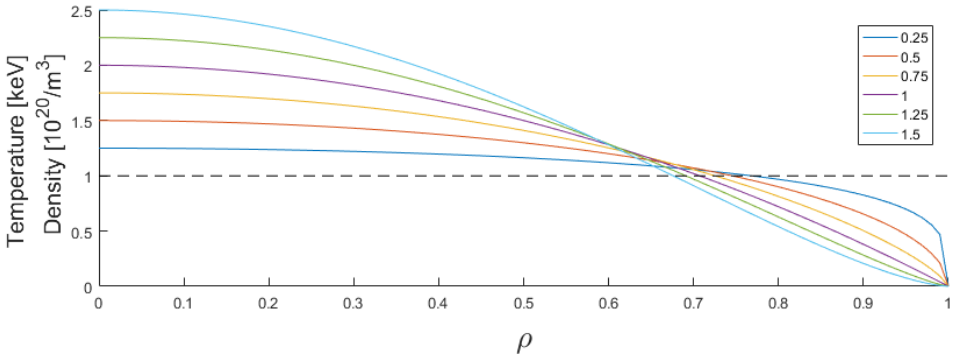


Figure 3.4: Plasma parameter profiles with the same volume-averaged temperature (1keV) or density $(10^{20}/m^3)$ with different $s_\Phi$ .

This reconciliation between the volume-averaged quantities and their associated profiles helps when calculating terms such as line radiation, which are highly effected by the the plasma's density and temperature profiles. This is especially relevant if impurities have entered the plasma which all TDAs account for to varying degrees. For example, a fusion plasma can contain a significant fraction of the first wall material, often up to 2% [50].

### 3.1.5 Steady State Conditions

All of the TDAs assume that the plasma is at a stable density, temperature and helium fraction. How each TDA applies these conditions is achieved in a variety of ways. The simplest method is to set a suitable helium fraction and maintaining it throughout. A more complex method involves solving the plasma power balance (equation (3.1)) with $\frac{dW}{dt} = 0$ in conjunction with the helium ash particle balance:

$$\frac{dn_{He}}{dt} = n_d n_t \langle \sigma v \rangle - \frac{n_{He}}{\tau_p} = 0 \tag{3.11}$$

where $n_d$, $n_t$ and $n_{He}$ are the particle densities of deuterium, tritium and helium respectively and $\tau_p$ is the particle confinement time. Due to the experimentally observed link between the particle diffusivity ($D$) and the thermal conductivity ($\psi$), it can be assumed that $\tau_p \propto \tau_e$. Based on the work of Becker et al. [65], transport simulations have shown that:

$$5 < \frac{\tau_p}{\tau_e} < 10 \tag{3.12}$$

although values as high as 30 were recorded during experiments on TEXTOR [66]. The work of Jakobs et al. [67] has shown that an upper limit for an ignited fusion plasma of $\frac{\tau_p}{\tau_e} \approx 15$. For this work, it is assumed that $\frac{\tau_p}{\tau_e} = 5$ as this is assumed for the design of ITER [50].

One of the consequences of assuming steady state conditions as part of the design process is that it puts a lower limit on the tokamak's pulse length. Based on D. Meade [68], the pulse length of a burning plasma experiment needs to be sufficient for the pressure profile to equilibrate whilst being alpha particle heated and the helium ash to accumulate for $5\tau_p$. As the NPGX also relies on a significant bootstrap current fraction(see section 3.1.7), there is also a requirement for the NPGX's current profile to be at least partially equilibrated. The minimum pulse length for the NPGX is therefore defined:

$$t_{pulse} \geq \tau_{pr} \text{ OR } t_{pulse} \geq \tau_{cr} \tag{3.13}$$

where $\tau_{pr} = 5\tau_p \, (= 25\tau_E)$ is the pressure profile relaxation time and $\tau_{cr}$ is the characteristic time scale of current profile equilibration at constant plasma current. $\tau_{cr}$ can be calculated based on [69]:

$$\tau_{cr}^{[s]} = 0.21 R_0^{[m]} I_p^{[MA]} / V_{loop}^{[V]} \tag{3.14}$$

where $V_{loop}$ is the equilibrium loop voltage of the plasma. Based on data from the ITPA Database[53], for a typical JET tokamak discharge, $V_{loop}$=0.1V and $\tau_E = 0.5$s. This would give $\tau_{pr} = 12.5$s and $\tau_{cr} = 16.4$s and values of the same order of magnitude are expected for the NPGX.

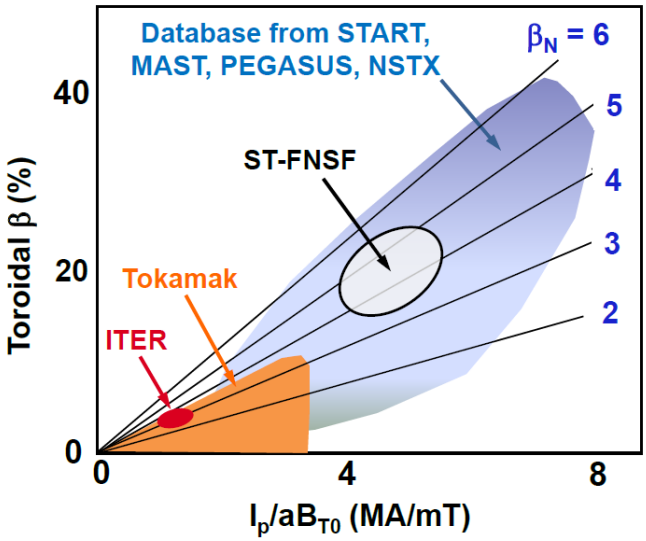


Figure 3.5: Graph of toroidal beta $\beta_t$ vs the normalized current $\frac{I_p}{aB_0}$ achieved on STs (NSTX, MAST, Pegasus and START), Conventional Tokamaks (orange), ITER's target (red) and the target of the ST-based Fusion Nuclear Science Facility (ST-FNSF) described in Menard et al. [33].

### 3.1.6 Operational Limits

All the considered TDAs use experimentally defined limits to define the peak operation of a tokamak. The first of these is the pressure limit as defined by F. Troyon et al. [70] used to avoid low toroidal mode number plasma instabilities:

$$\beta_t \leq \beta_{t,crit} = \beta_{N,max} \frac{I_p^{[MA]}}{a^{[m]} B_0^{[T]}} \tag{3.15}$$

where $\beta_t = \frac{2\mu_0 \langle p \rangle}{B_0^2}$ and $\beta_{N,max}$ is the normalized beta and has been determined by experiments. A value of $\beta_{N,max} \leq 2.8 - 4.0$ is used by most TDAs but some TDAs allow for an aspect ratio dependent $\beta_{N,max}$. This aspect ratio dependence allows for the experimental results on STs suggesting that $\beta_{N,max} \approx 6$ can be achieved (figure 3.5) [71]. One example used by the TESC is [51]:

$$\beta_{N,Max} = \frac{9}{A} \tag{3.16}$$

The second is the density limit as defined by Greenwald et al. [72]:

$$n_e < n_{gw} \left[ \frac{10^{20}}{m^3} \right] = \frac{I_{p,[MA]}}{\pi a_{[m]}^2} \tag{3.17}$$

Exceeding this limit leads to a disruption although the mechanism that leads to this disruption is not well understood [73]. Experiments have shown that, even without exceeding this limit, approaching it leads to a degradation in energy confinement of the plasma [24].

The third limit is the kink instability limit as defined by $q^* \leq q^*_{crit}$. The precise formula that defines this limit varies for different TDA. For the purposes

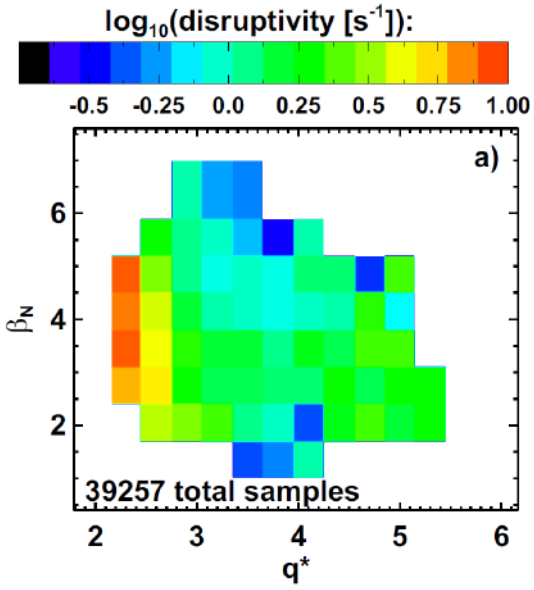


Figure 3.6: NSTX plasma disruptivity for varying $\beta_N$ and $q^*$ [33]

of this work, the expression defined by Menard et al. [33] will be used as it was defined based on NSTX data:

$$q^* = \frac{\pi a^2 B_0}{\mu_0 R_0 I_p}(1+\kappa^2) \leq q^*_{crit} \tag{3.18}$$

where $q^*_{crit} \geq 3$.is required to ensure low disruptivity assess to high $\beta_N$ plasma, as illustrated in figure 3.6.

The final limit is the neutron wall loading of the vacuum vessel ($n_w$). Neutrons released by fusion reactions bombard the walls of the vacuum vessel depositing their heat and this can potentially cause issues. All the considered TDAs chose a limit for the neutron wall loading that falls in the range from $1[MW/m^2]$[33] to $5[MW/m^2]$[74]. For this work, the same limit chosen by the ARIES system code is to be used [37]:

$$n_w \leq 4[MW/m^2] \tag{3.19}$$

### 3.1.7 Bootstrap Current

Soon after the Bootstrap current ($I_{bs}$) was theorized in 1967 [75], it was foreseen that this pressure-gradient driven toroidal current could be used to allow the steady state operation of tokamaks [76]. The first evidence of the Bootstrap Current was published in 1988[77], but since then many other tokamaks have now recorded significant bootstrap currents, some recording bootstrap fractions ($f_{bs} = \frac{I_{bs}}{I_p}$) approaching 100% [78].

The most recent published work on how to predict bootstrap fraction from tokamak parameters is that of Andrade et al. [79]. A theoretical analysis was performed to produce the following scaling law for bootstrap fraction that was then fit to experiment results (see figure 3.7):

$$f_{bs}^{[\%]} = 5 C_{bs} A^{0.5} \frac{(1+s_n+s_t)\beta_N^{[\%]}\, q^{cyl}\kappa}{l_i^{1.20}} \frac{R_0}{R_m} \tag{3.20}$$

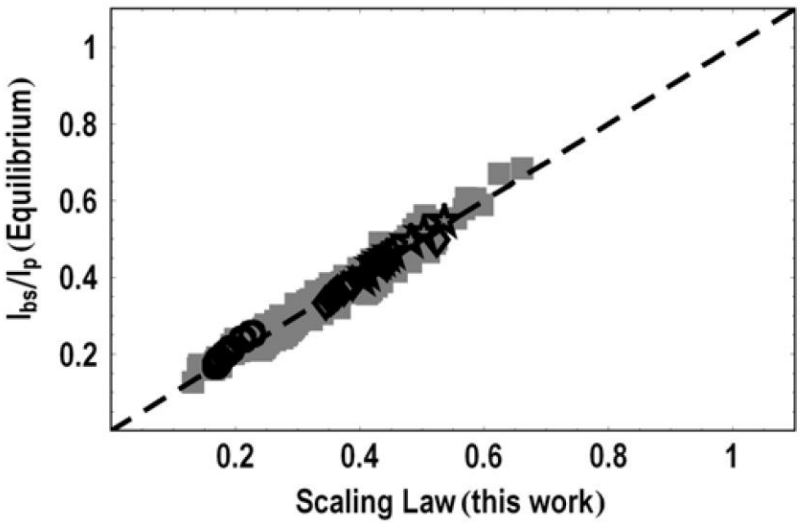


Figure 3.7: The fit of equation (3.20) to a database of equilibrium data for the ETE tokamak consisting of 347 points [79].

where $q^{cyl} = \frac{2\pi a^2 B_0}{\mu_0 R_0 I_p}$, $C_{bs}$ is a constant determined by fitting to experiment data, $l_i$ is the normalized internal inductance of the plasma and $R_m$ is the major radius of the magnetic center of the plasma.

Knowing $f_{bs}$ allows the required amount of driven current ($I_{CD}$) to be determined. In a tokamak, this current is traditionally driven by a central solenoid using induction but it can also be driven by non-inductive means.

### 3.1.8 L-H mode transition

In section 3.1.2 it was shown that the degree of energy confinement in the plasma has a big impact on the plasma's ability to sustain fusion reactions. Experiments have shown that the degree of energy confinement is improved by ensuring a consistent amount of plasma energy is lost over the LCFS ($P_{LCFS}$). Sustaining this rate of energy loss results in the formation of an energy transport barrier at the plasma's edge that greatly improves the plasma's overall energy confinement. The formation of this edge transport barrier (ETB) marks the point where the plasma starts to operate in its high confinement mode, also known as 'H-mode'. As all the considered TDAs assume operation in this mode, this mode is assumed for the NGPX and the dynamics of entering H-mode have to be considered. Experiments have shown that H-mode's characteristic ETB forms when the power crossing the LCFS exceeds some critical level:

$$P_{LCFS} \quad \geq \quad P_{L-H}\,(1 + \text{'RMSE'}) \tag{3.21}$$

where $P_{LCFS} = P_{aux} + P_\alpha + P_\Omega - \frac{dW}{dt}$ and 'RMSE' is the root-mean-squared-error of the expression used to calculate $P_{L-H}$. As there is no current first-principles explanation to explain the formation of this ETB, a database of L-H transition data has been built up [80]. As the database was expanded, empirical laws were developed [80, 81, 82, 83, 84], all of which had a similar RMSE ($\approx 30\%$) at the time they were developed. For the purposes of this work, the scaling law developed by Takizuka T. el al. [81] is used because it accounts for the most

plasma parameters and includes an aspect ratio dependence:

$$P_{L-H[MW]} = 0.072\ {n_{e,20}^{-}}^{0.7}\ B_{0[T]}^{0.7}\ S_{p[m^2]}^{0.9}\left(\frac{Z_{eff}}{2}\right)^{0.7}\left(\frac{0.1A}{1-(\frac{2}{1+A})^{0.5}}\right)^{0.5} \tag{3.22}$$

where $S_p = 4\pi^2 a R_0\left(\frac{1+\kappa^2}{2}\right)^{0.5}$.

### 3.1.9 Divertor

The divertor can be considered the exhaust of a tokamak. All the thermal energy and particles that crosses the LCFS flow along magnetic field lines to the divertor. This parallel transport is a fast process when compared to the particle transport perpendicular to the field line and this can result in a large amount of thermal energy being deposited on a small area of divertor material, known as the divertor strike point. A capable divertor therefore needs to be able to accept this heat load without material failure.

Divertor tile heat loads on ITER have been estimated to be $\approx 10[MW/m^2]$ [45] and heats loads on the divertors of STs could be higher due to their smaller size. All the considered TDAs make some attempt to determine divertor heat loads but tend to rely heavily on radiative cooling of the divertor plasma by operating in a detached divertor plasma regime [45].

By using the assumption of a detached divertor plasma, all the TDAs avoid the need to investigate the other key damage mechanisms of the divertor. The most significant of these mechanisms is physical sputtering, the process by which plasma ions knock out atoms of the divertor surface, leading to erosion of divertor material and contamination of the bulk plasma.

Inspired by the large number of assumptions made by the considered TDAs, a more rigorous approach to estimating divertor heat load was formulated based on the work of Eich et al. [85]. This is described in section 4.3.

### 3.1.10 Neutral Beam Injection

As shown in section 2.3, the cost investigation requires the NPGX's beam energy ($E_{beam}$) and beam power ($P_{aux}$) to be quantified as the former is used to determine whether PNBI or more costly NNBI is required and the latter is the volumetric cost indicator. The maximum energy for the PNBI is set as 130kev/D as a PNBI system of this energy has been successfully used on JET[47].

Evaluating $E_{beam}$ requires an analysis of how neutral particles entering the plasma interact with bulk plasma particles to become ionized. The reaction cross-section of the most dominant processes - charge exchange $\sigma_{CX}$, proton impact ionization $\sigma_p$ and electron impact ionization $\sigma_e$ - are shown in figure 3.8. These quantities can be used to predict the beam's intensity ($I_b$) as it progresses through the plasma using the following expression[9]:

$$\frac{I_b(l)}{I_{b0}} = \exp\left\{-\int_0^l \sigma_{Tot}(E_{beam})\ n_e(l)\ dl\right\} \tag{3.23}$$

where $l$ is the distance along the center line of the beam path, $I_{b0}$ is the beam intensity at the location where the beam enters the plasma, $\sigma_{Tot}$ is the total reaction

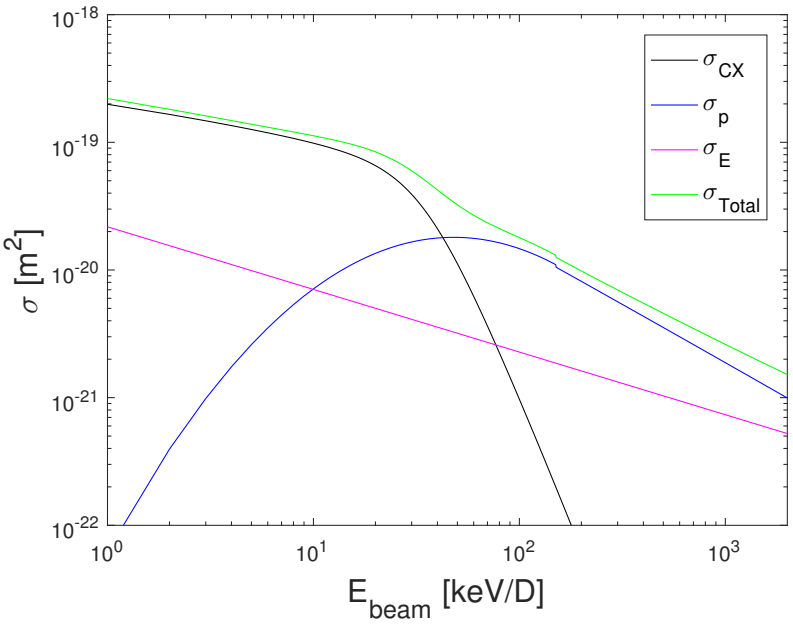


Figure 3.8: Relevant ionization reaction cross sections for a neutral deuterium beam traversing a plasma: $\sigma_{CX}$: charge exchange[87]; $\sigma_p$: proton impact ionization[87] and $\sigma_E$: electron impact ionization[88].

cross-section (shown in figure 3.8) and $n_e$ is the electron density. Determining an appropriate $E_{beam}$ can be achieved by evaluating equation (3.23) along the required beam path. This requires knowledge of how the plasma's electron density varies along the beam path, which are functions of the volume-average electron density and the density profile peaking factor, and the beam line orientation - either perpendicular to the plasma surface or tangential. Tangential injection beams can also be aimed at a location offset from the plasma's geometric center as this has been found to improve current drive efficiency[86].

## 3.2 Engineering Investigation

At the simplest level, any tokamak needs to provide sufficient toroidal field and plasma current to provide the conditions for sustained DT fusion. In section 3.1, the relevant tokamak plasma physics was introduced. These physics requirements indicate that increasing a tokamak's toroidal field allows access to larger stable plasma currents, leading to better energy confinement, access to higher plasma pressures and a more efficient device. However, the toroidal field strength is limited by what can be achieved with the available materials.

In this section, the engineering aspects of tokamak design are introduced within the context of the NPGX experiment. This covers aspects of the TF coil topology, the TF coil's principle limits and the factors that govern the tokamak's poloidal layout. (Readers are referred to appendix C for the material properties of OFCu collected from [89, 90]).

### 3.2.1 TF Coil Topology - Constant Tension Curve

The NPGX's TF coil is to consist of a single common centerpost coupled to a yet-undetermined number of return limbs ($N_{limbs}$) whose topology is to be based on a constant tension curve (CTC). This is a robust choice as CTC-based TF limbs are designed to avoid stress concentrations and out-of-balance forces in the poloidal plane by accounting for the variation in the toroidal magnetic field strength along the limb's path. They also tend to be cheaper than alternatives, such as the picture frame coil, as they require less material volume and have lower self-inductance.

The theory governing the design of CTC-based TF coil assumes that each limb is an up-down symmetric curved length of rigid conductor which is carrying current in the external magnetic field produced the centerpost. For the case of the NPGX TF coil, the centerpost can be assumed to be an infinite straight wire and the return limb a section of a current carrying ring. This allows the tension due to Lorentz forces in a return limb ($T$) to be expressed as:

$$T = I_{coil} B_{ext} p \tag{3.24}$$

where $I_{coil,[A]}$ is the current in the coil, $B_{ext,[T]}$ is the magnetic field strength applied to the coil and $p_{[m]}$ is the radius of curvature of the return limb.The magnitude of $B_{ext}$ produced by an the centerpost can be calculated using the expression:

$$B_{ext} = \frac{B_0 R_0}{R} \tag{3.25}$$

where $B_0$ is the magnetic field strength at the radius $R_0$ and $R$ is the radius where $B_{ext}$ is calculated with respect to the centerpost's central axis. Combining equation (3.24) and equation (3.25) and making the radius of curvature of the return limb a linear function of $R$ ($p = C\ R$) gives:

$$T = I_{coil} B_0 R_0 C \tag{3.26}$$

where 'C' must be kept constant along the return limbs to ensure the tension is constant. This restriction on 'C' allows a CTC to be drawn as a function of its

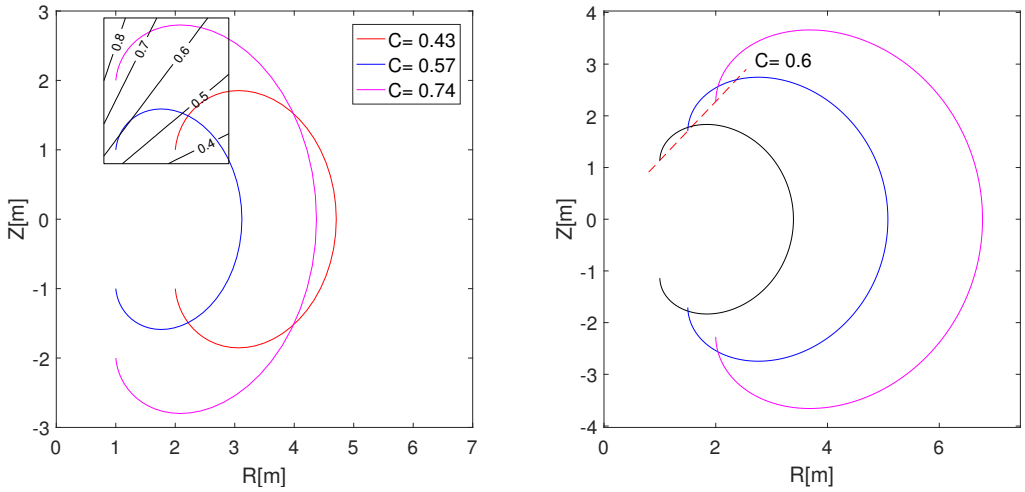


Figure 3.9: Left: 3 CTC with starting locations $(R_s, Z_s)$ = (2,1) red, (1,1) blue and (1,2) magenta. Inset shows the contours of equal 'C' in the range ($0.8 < R < 2.9$, $0.8 < Z < 2.9$). Right: 3 CTCs with equal 'C' but different starting locations.

starting location $(R_s, Z_s)$ using the following iterative expression for $1 \leq n \leq N$ where $N \in \mathbb{R}$, $\Delta\theta = 2\pi/N$, $\theta = \Delta\theta n$ and $(R_0, Z_0) = (R_s, Z_s)$:

$$\begin{aligned} S_n &= R_{n-1} + C\, R_{n-1}\, \Delta\theta\, \sin(\theta) \\ R_n &= R_{n-1} + \left(\frac{1}{2}\, C\, \Delta\theta\, (R_{n-1} + S_n)\right) \sin(\theta + \frac{1}{2}\Delta\theta) \\ Z_n &= Z_{n-1} + \left(\frac{1}{2}\, C\, \Delta\theta\, (R_{n-1} + S_n)\right) \cos(\theta + \frac{1}{2}\Delta\theta) \end{aligned} \tag{3.27}$$

In turn, equation (3.27) can be iterated for varying 'C' until an up-down symmetric CTC about the centerpost axis results.

Equation (3.26) and equation (3.27) puts restrictions on the TF coil topology that require its position to be determined as a function of the size and shape of the tokamak's components that are to placed inside it. As these are themselves functions of other tokamak parameters (see section 3.2.5), it can be illuminating to determine how 'C' varies for different $(R_s, Z_s)$, which is depicted in figure 3.9. The figure shows that a CTC-based return limbs gets less resistant to high coil current as its starting location moves to increasing $Z_s$ and/or decreasing $R_s$ and that there are multiple choices for the starting location of the CTC which are equally capable of withstanding high coil current.

### 3.2.2 Principal Limits - Temperature Rise

The TF coils of a DT fusion-capable tokamak are subject to two heat loads which limit the length of time the TF coil can operate. These heat loads are discussed in this subsection.

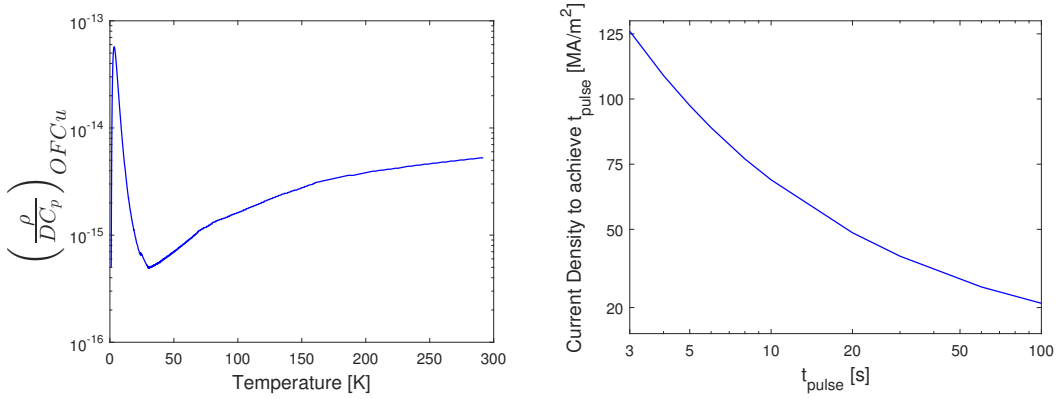


Figure 3.10: Left: How $\frac{\rho}{DC_p}$ for OCFu varying with temperature based on data from [89], Right: Limit of centerpost current density $J_{rod}$ to ensure a given pulse length ($t_{pulse}$). Assumes Adiabatic heating of TF coil from 80-180K with constant current

### Ohmic Heating

The first is the resistive heating of TF coils ($P_{\Omega,TF}$). This occurs in any conductor with finite resistivity such as the OFCu that will be used on the NPGX. Assuming an adiabatic heating process, the temperature rise of the TF coils becomes a function of the OFCu's ability to store heat energy. This results in the following expression for temperature rise:

$$\left(\frac{dT}{dt}\right)_{OFCu} = J^2 \frac{\rho}{DC_p} \tag{3.28}$$

where $J$ is the current density through the OFCu and $\rho$, $D$ and $C_p$ are the electrical resistivity, density and specific heat capacity of the OFCu respectively. How $\frac{\rho}{DC_p}$ varies with temperature is shown in figure 3.10, left. This function was used to determine the timed temperature rise in the TF coils when subjected to different current densities. Based on an allowed temperature rise of 100K (80K-180K), a maximum current density through the centerpost ($J_{rod}$) can be determined that would allow a specified pulse length. This is shown in figure 3.10, right.

### Neutron Heating

The pulse lengths depicted in figure 3.10, right are the maximum pulse lengths that can be achieve for given coil current density if it was not for the heat load on the TF coils due to neutrons bombardment ($P_{n,TF}$). Unfettered neutron bombardment of the TF coils, especially in the volume of the centerpost, would result in a large amount of heat deposition in the TF coils and to avoid this the NPGX will utilize neutron shielding between the plasma and the centerpost. To avoid need for iteration with the mechanical design, the neutron shield is designed in order to reduce the flux of fast neutrons ($E > 0.1$MeV) by $\approx 95\%$. Achieving this level of reduction allows the assumption: $P_{n,TF} \ll P_{\Omega,TF}$ and therefore the pulse length will only be limited by the ohmic heating of the centerpost, as depicted in figure 3.10.

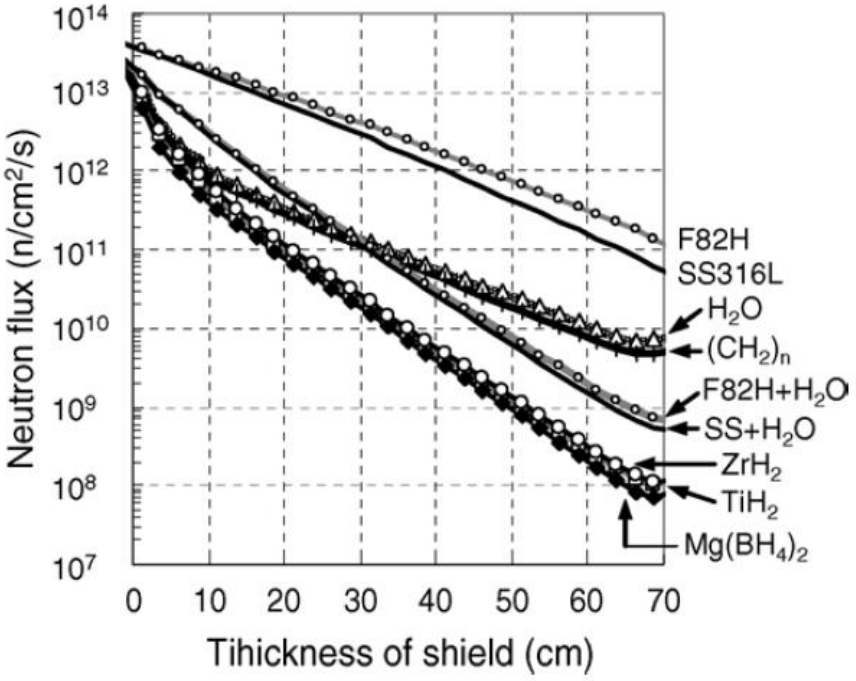


Figure 3.11: Attenuations of fast neutron fluxes (above 0.1MeV) in the outboard shield of the JAERI DEMO tokamak concept for shield materials. Reprinted from [91].

In order to achieve the required reduction is fast neutron flux, a neutron shield that can efficiently absorb the energy of neutrons over as short as possible distance is required. Materials that are efficient absorbers of neutron energy are known as moderators. Based on T. Hayashi [91], the material magnesium borohydride ($Mg(BH_4)_2$) is to used as the NPGX's moderator due to its high hydrogen number density ($1.32 \times 10^{29}[H/m^3]$)[2]. As shown in figure 3.11, over a thickness of $Mg(BH_4)_2$ of $\approx$ 8cm, the flux of fast neutrons drops from $\approx 10^{13}$ to $5{\times}10^{11}$ [n/cm$^2$/s]. This is sufficient to achieve the required reduction in fast neutron flux required by the NPGX.

Based on this minimum moderator thickness, the NPGX's centerpost, neutron shield, plasma-facing components and support structure geometry was defined as shown in figure 3.12. The gap between plasma's inside edge and the centerpost is therefore 13.5cm.

A secondary effect of neutron bombardment is the degradation of the OFCu's material properties. Based on data calculated during the conceptual design for a component test facility based on an ST (CTF-ST) [92], the CTF-ST's centerpost suffers irradiated damage at a rate of $\approx$ 0.102 dpa per MW-year of fusion power produced by the plasma. OFCu starts to become embrittled after only 0.01 dpa of neutron damage[92] and therefore, assuming the same damage rate, the NGPX would not suffer significant material degradation until it has produced 0.1MWy of fusion power. This gives the NPGX an indicative useful life of $\approx$ 3100 DT plasma pulses assuming the production of 100MW of fusion power for 10 seconds during each pulse.

[2]Compared to $H_2O$: $6.7 \times 10^{28}[H/m^3]$

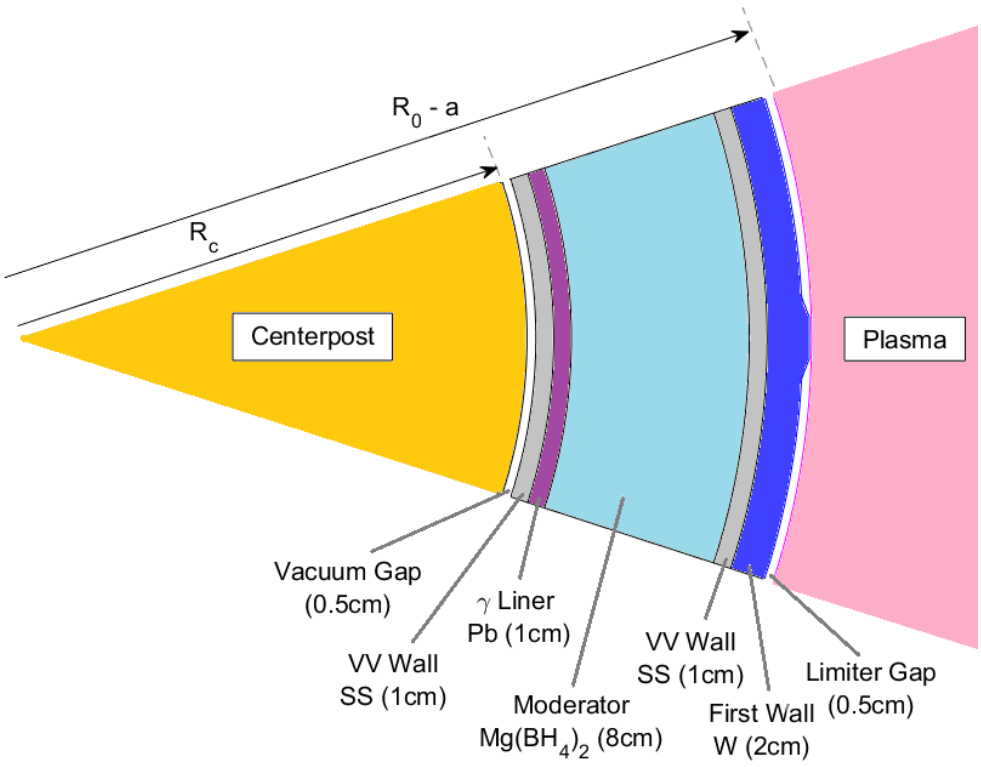


Figure 3.12: Top-down view of a section of the NPGX between the centerpost and the plasma showing the rough arrangement of the neutron shielding at the mid-plane. The area contains 2 vacuum vessel walls, one on the outer (plasma) side used as a mount for the first wall, the other of the inner (centerpost) side as a mounting for a gamma-radiation shield (lead). These VV walls together form a box to holds the moderator powder. A vacuum gap between the inner VV wall and the centerpost is provided by the outer vacuum chamber that surrounds the whole tokamak and is used to reduce heat transfer to the centerpost.

### 3.2.3 Principal Limits - Yield Stress

Although there are many sources of stress on a tokamak's TF coils, the first stage design of a TF coil is governed by just two. These two forces and how to avoid material failure in the TF coils are the subject of this subsection.

Both of the induced forces are Lorentz forces caused by the current flow interacting with a magnetic field. The first, introduced earlier in section 3.2.1, is the resultant tension force on the centerpost due to the Lorentz forces in the limbs. This force acts along the longitudinal axis of the centerpost resulting in it extending vertically. The second is the compressive pinching force in the centerpost induced by the current flowing along the centerpost interacting with its self-field. This force acts radially towards the center of the centerpost and, due to the Poisson effect, also results in a longitudinal extension of the centerpost.

It is assumed for this work that failure of the centerpost due to plastic deformation needs to be avoided. The onset of this failure mode can be determined by comparing the yield stress ($\sigma_y$) of OFCu to the von Mises stress ($\sigma_{VM}$) [93]:

$$\sigma_{VM} = \left[\frac{1}{2}\left((\sigma_1 - \sigma_2)^2 + (\sigma_2 - \sigma_3)^2 + (\sigma_3 - \sigma_1)^2\right)\right]^{\frac{1}{2}} \tag{3.29}$$

where $\sigma_{1,2,3}$ are the principle stresses in the directions of the three principle axes. To avoid plastic deformation, $\sigma_{VM} \leq \sigma_y$. As the compressive pinch pressure and limb tension stress are in perpendicular directions, they each lie on different principle directions. As one is compressive and the other tensile, their magnitudes add when evaluating the von Mises stress.

The stress-strain curves for 60% hard OFCu at various temperatures (see C, [90]) was used to determine OFCu's yield stress. The results are shown in figure 3.13. This implies that a yield stress limit for the TF coil based on the lowest value in the allowed operating temperature range: 319[MPa]. As it is not customary to operate near the yield stress of material if plastic deformation is to be avoided, a safety factor of 20% has been applied, giving a design stress limit ($\sigma_{VM} \leq \sigma_{d,lim}$) to 250[MPa].

### 3.2.4 TF Power Supplies

This section focuses on the engineering issues relevant to providing current to the TF coil from super-capacitor banks. The goal is to determine a method of calculating the number of super-capacitors ($N_{SC}$) needed to provide a given centerpost current ($I_{rod}$) for a given pulse length ($t_{pulse}$).

The first stage of this analysis uses a simplified model of the electrical energy balance of the TF coil circuit. This model equates the electrical energy required to raise and maintain the limb current ($I_{limb}$) to the total energy stored in each coil's capacitor banks ($W_{bank}$):

$$W_{bank} = I_{limb}^2(R_{TF}t_{pulse} + \frac{1}{2}L_{TF}) \tag{3.30}$$

where $L_{TF}$ and $R_{TF}$ are the inductance and resistance of each TF coil limb respectively. Equation (3.30) indicates that minimizing $W_{bank}$ for a given $I_{rod}$ requires

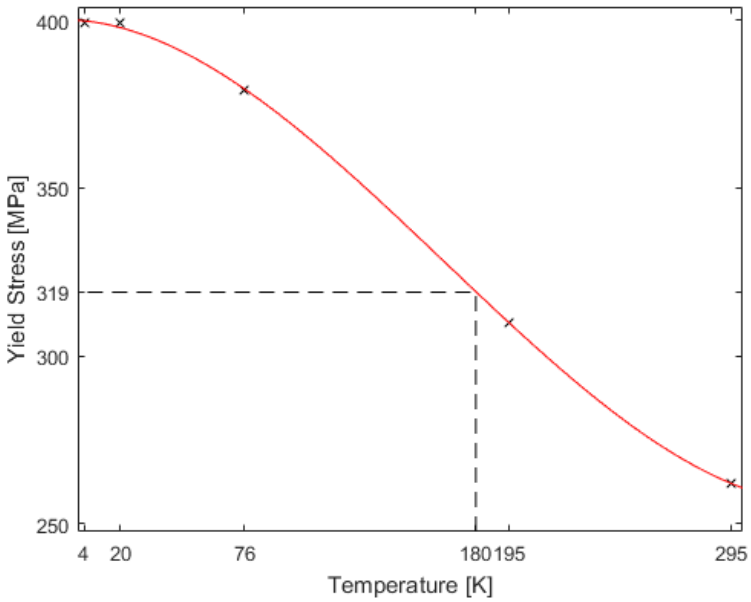


Figure 3.13: Yield Stress of 60% hard OFCu for temperature range 0-300[K]. Data points ('x') were used to determine a best fit line (red) from which the yield stress determination at other temperatures were made.

maximizing the number of return limbs ($I_{limb} = I_{rod}/N_{limbs}$) and minimizing $R_{TF}$ and $L_{TF}$.

Estimating the relative magnitude of $R_{TF}$ and $L_{TF}$ allows an order of design precedence to be set. The basis of this determination uses the simple example of a square toroidal coil of 'N' turns. The resulting expressions for $R_{TF}$ and $L_{TF}$ for a single coil that makes up part of a toroidal solenoid are derived from formulae in [94]:

$$R_{TF} = \frac{\rho[2(b-a)+2h]}{A_{coil}} \tag{3.31}$$

$$L_{TF} = h\frac{\mu_0 N}{2\pi} ln\frac{b}{a} \tag{3.32}$$

where 'a' and 'b' are the radii of the inner and outer extent of the coil, 'h' is the height of the coil, $A_{TF}$ is the coil's cross sectional area. Inserting typical values for a LN2 cooled ST TF coil ($\rho = 2 \times 10^{-9}\ \Omega m, a = 0.2m, b = 3m, h = 6m, N = 24, A_{coil} = 0.1m^2$) gives $R_{TF} = 0.352 \times 10^{-6}\Omega$ and $L_{TF} = 78 \times 10^{-6}H$. As $L_{TF} > R_{TF}$, optimizing the TF coil design requires $L_{TF}$ to be as small as possible unless $t_{pulse}$ becomes large ($\geq$ 100s). In the case of a TF coil, this is equivalent to minimizing the height (h) and radial extent (b) of the coil by the appropriate selection of ($R_s$,$Z_s$) for the CTC. Minimizing 'h' and 'b' also helps to reduce $V_{Cu,TF}$. The engineering model therefore needs to define a TF coil that is as small as possible, provides the required magnetic field ($B_0$) and contains the plasma and supporting equipment.

### 3.2.5 Tokamak Radial Build

In this section, the radial build of the NPGX is considered. This includes the determination of relevant TF coil dimensions and an examination of which NPGX

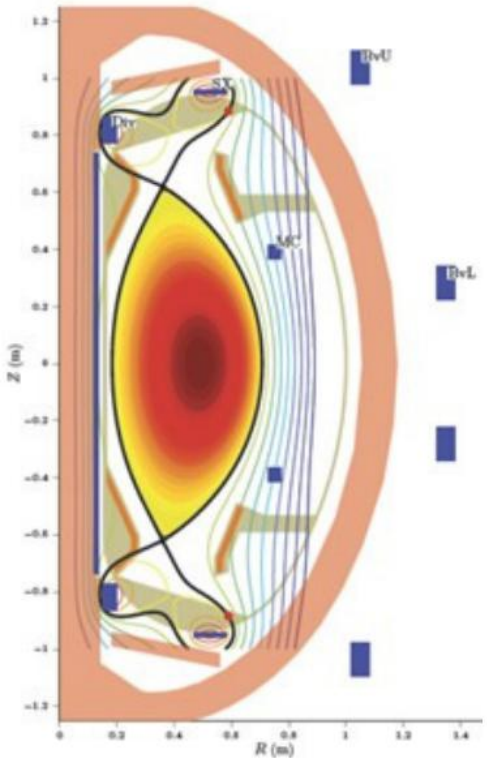


Figure 3.14: MHD equilibrium from FIESTA code showing the poloidal cross section of TE's ST40 tokamak. Shown is the TF coil (brown), vacuum vessel (green) and coil locations (blue). This shows that ST40's TF coils surround the plasma, vacuum vessel, divertor, divertor plasma shaping coils and the merging compression coils [95].

components effect the starting location of the TF limb CTC.

As eluded to in section 3.2.1, the return limbs of the NPGX are to follow a path determined by a CTC. As the cross-sectional area of the centerpost ($A_{cp}$) is set by NPGX properties which are independent variables, the temperature rise of the centerpost is, in a sense, a predetermined limiting factor during a pulse. In order not to limit the TF coil further, the cross-sectional area of the limb ($A_{limb}$) need to be sufficiently large so that its temperature does not rise faster than the centerpost (see equation (3.28)). As each limb only carries a fraction of $I_{rod}$:

$$A_{limb} \geq A_{cp}/N_{limbs} \tag{3.33}$$

TE's ST40 uses a rectangular limb cross-section so this is assumed for the NPGX.

Another effect of designing a TF coil to have minimum radial and vertical extent is that only essential components should be placed inside the TF. As the NPGX is to share many similarities to TE's ST40 tokamak, ST40 was examined and figure 3.14 shows its radial build. Besides the plasma and vacuum vessel, ST40's TF coils surround coils for divertor shaping and the merging compression plasma initiation system. As the NPGX is to use these same systems, it can be reasoned from the figure that the position of the innermost divertor shaping coil and the merging compression coils and its surrounding vacuum vessel structure are features that would define the shape of the NPGX's TF coils.

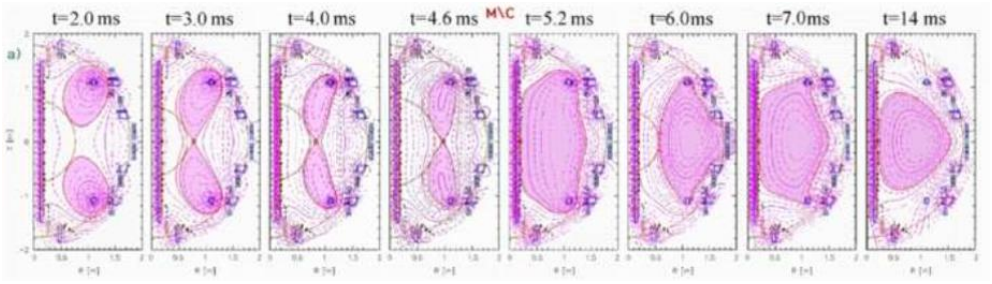


Figure 3.15: Merging Compression achieved on MAST (reprinted with permission [96])

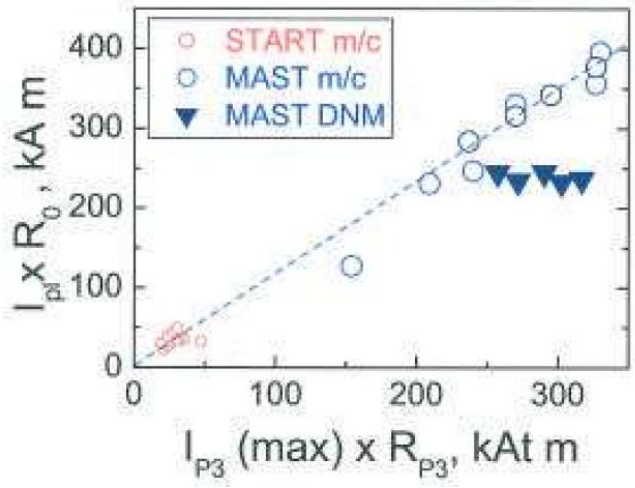


Figure 3.16: Plasma current vs. merging compression coil (P3) current for START and MAST experiments (normalized to R0 and the MC coil radius) (reprinted with permission from [96]).

The inner divertor coil on ST40 is positioned just outside the vacuum vessel adjacent to the inner divertor strike surface. Its primary task to create the divertor X-point and therefore its coil current during operation needs to be a significant proportion of the plasma current. Based on ST40's divertor coil, the NPGX's divertor coil should be designed to carry $\approx \frac{1}{3} I_p$. The minimum starting height of the NPGX's CTC is therefore a function of the plasma height ($\kappa a$), the gap to the inner divertor strike surface, the gap to the bottom of the divertor coil and the size and shape of the divertor coil.

The NPGX's merging compression (MC) start-up system is to be used to quickly initiate the plasma. Merging compression works by pulsing a high current through 2 up-down symmetric coils inside the vacuum chamber. This has been shown to create tokamak plasma of high temperature with an induced current proportional to the current pulsed through the merging compression coil [96]. As there is no planned central solenoid in the NPGX, the merging compression plasma initiation system needs to be designed to achieve the rated plasma current.

# 4. Model Definition

In section 2, a cost model was defined based on the volumetric cost indicators ($V_{OFCu}$, $N_{SC}$, $P_{PNBI}$, $P_{NNBI}$). In section 3, an investigation into the physics and engineering issues inherent in ST design was presented. This included operational limits based on plasma physics as well as the physical limitations on the engineering design.

In this section, this background information is used to build models that can determine under what conditions a plasma of a certain size and shape can achieve $Q_{fus} \geq 2.5$ and, assuming these conditions are achievable, how much achieving $Q_{fus} \geq 2.5$ might cost.

## 4.1 Physics Model

Based on physics described in section 3, a number of assumptions can be made about ST plasmas. These are shown in table 4.1 along with the reference(s) on which they are based.

Of the assumptions shown in table 4.1, a few require a modicum of explanation. The first is the design choice to use the PETTY08 scaling to calculation $\tau_E$. This choice was made due to recent work by Sips et al. [97] implying that the energy confinement enhancement with respect to the ITER98(y,2) scaling ($H_{98y2}$) on several tokamaks may have a $\beta_N$ dependence (see figure 4.1) . Although it does not prove either scaling more or less accurate, it does imply that the $\beta$-dependence of the ITER98(y,2) scaling may be incorrect. That said, due to the inaccuracies inherent in calculating $\tau_E$ from both these scalings ($\pm 14\%$ [45, 52]), the PETTY08 scaling is to be used but the resulting energy confinement enhancements from the other scalings in table 3.1 are to be monitored.

The second noteworthy assumption is the use of an energy enhancement factor ($H_f$) of 1.5 relative to the beta-independent PETTY08 scaling. This is justified for the NPGX as A. Costley et al. [51], in their 2015 paper, imply that this degree is energy confinement enhancement has been demonstrated in 'many smaller devices than have provided data' to the ITPA database [53]. This is backed up by

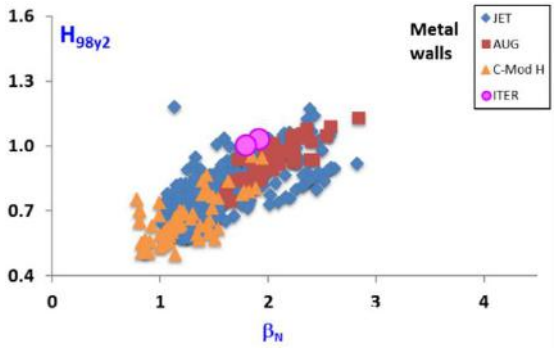


Figure 4.1: Comparing devices with metal walls with respect to the normalized H-mode energy confinement enhancement factor relative to the ITER98(y,2) scaling (H98y2) as a function of $\beta_N$ (from Sips et al. [97]).

Table 4.1: List of Assumed Physics Parameters for Physics Investigation

| **Parameter** | Symbol | **Value** | **Citation** |
|---|---|---|---|
| Confinement Scaling | - | PETTY | DC[1] |
| Energy Enhancement Factor | $H_f$ | 1.5 | [51] / [55] |
| Design Plasma Triangularity | $\delta$ | 0.5 | DC[1] / [62] |
| Minimum Kink Safety Factor | $q*$ | 3 | [33] |
| Density Peaking Factor | $s_n$ | 0.5 | [51] |
| Temperature Peaking Factor | $s_t$ | 1.5 | [51] |
| Particle Confinement Time | $\tau_p$ | $5\tau_e$ | [50] |
| Minimum Pulse Length | $t_{pulse}$ | $5\tau_p$ / $\tau_{cr}$ | [68] |
| - | $C_{bs}$ | 0.1558 | [79] |
| Normalized Internal Inductance | $l_i$ | 0.5 | [33] |
| Geometric-Magnetic Plasma Center Ratio | $R_0/R_m$ | 0.8 | [33] |
| Impurity Fraction (First Wall) | $f_{FW}$ | 2% | [50] |
| Impurity Charge (First Wall) | $Z_{FW}$ | 3 | [60] |
| Impurity Atomic Mass (First Wall) | $A_{FW}$ | 6.94 | [60] |
| Alpha Power absorption fraction | $f_\alpha$ | 0.95 | [98] |
| Reflectivity of the Wall | $R_f$ | 0.7 | [51] |
| Normalized Current Drive Efficiency | $\gamma_{CD}$ | 0.5 | [99] / [51] |

1: 'DC': Design Choice

the NPGX's use of a Lithium coated first wall and that energy enhancement factors at this level were recorded during energy confinement studies on the MAST spherical tokamak [55].

Based on the assumptions of table 4.1, an ST plasma can be defined using only ($R_0$, A). The capabilities of the plasma, however, required the magnitude of the toroidal field (characterized by $B_0$) and the plasma current ($I_p$) to be specified. As the allowable combinations of $B_0$ and $I_p$ are restricted to avoid kink instabilities, it is possible to determine $I_p$ from $B_0$ using equation (3.18).

With these parameters determined, the fusion power gain ($Q_{fus}$) and auxiliary heating power ($P_{aux}$) can be calculated by solving the plasma power and helium ash particle balance in steady state ($\frac{dW}{dt} = 0$ and $\frac{dn_{He}}{dt} = 0$) using equation (3.1) and equation (3.11) respectively for a range of plasma densities and temperatures.

As the NPGX has no planned solenoid, the range of plasma densities and temperatures is restricted to those that achieve close to the maximum bootstrap fraction ($f_{bs,Max}$). The bootstrap fraction $f_{bs}$ can be calculated using equation (3.20). Using the assumptions made in table 4.1, equation (3.20) becomes:

$$f_{bs}^{[\%]} = 78.939\ A^{-0.5}\ f_{\beta_{N,Max}}\ q^*\ \frac{\kappa}{1+\kappa^2} \tag{4.1}$$

where $f_{\beta_{N,Max}} = \beta_N/\beta_{N,Max}$. This indicates that to get high $f_{bs}$, the ST needs to operate at a high plasma pressure. To avoid the risk of disruptions, tokamaks tend to operate away for the pressure limit defined by $\beta_{N,Max}$. This work assumes a safety margin of 10% is sufficient to avoid disruptions resulting in $f_{\beta_{N,Max}} = 90\%$. It is also assumed that a 15% margin is required away from the Greenwald density limit, similar to the allowable Greenwald density fraction ($f_{gw} = n_E/n_{gw}$) on ITER[50]. Within these limits, the relevant operating densities and temperatures in ($n_e$,$T$) space can be defined - as shown by the red line in figure 4.2.

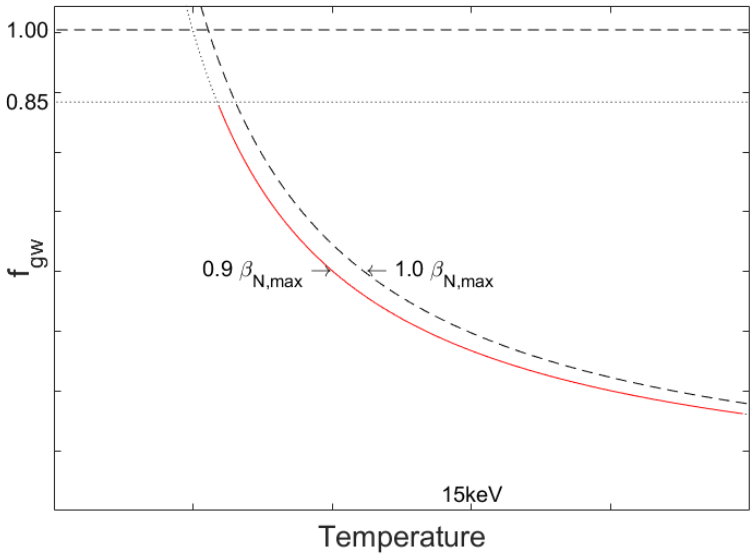


Figure 4.2: Example ($f_{gw}$, T) space plot showing the Greenwald density ($f_{gw} = 1$) and Troyon beta ($\beta_{N,Max}$) limits. Operating points of interest to the NPGX are shown is red where $n_e \leq 0.85\ n_{gw}$ and $\beta_N = 0.9\ \beta_{N,Max}$.

Another outcome of equation (4.1) is that $f_{bs} = f(q*, A)$. As the tokamak's aspect ratio is an independent variable, this implies that to achieve the required $f_{bs}$, $q^* = f(A)$ with the limit: $q^* \geq 3$. With $q^* = 3$, $I_p$ is at its maximum value for a given $B_0$ and $f_{bs} \approx 60\%$ for the range of aspect ratios being studied. Rising $f_{bs}$ to $\approx 90\%$ requires $q^* \approx 5$. The NPGX can choose to operate at either end of this scale, either maximizing $I_p(q* = 3)$ or $f_{bs}(q* \approx 5)$.

Calculation of the $f_{bs}$ has an impact on the manner to which the heating power is applied, splitting it into two categories: 1) to heat the plasma and 2) to drive current: $S_{aux} = S_{heat} + S_{CD}$. The power needed to drive all the leftover current non-inductively can be calculated using the following expression derived from [51, 99]:

$$S_{CD} = \frac{1}{V_p} I_p (1 - f_{bs}) \left( \frac{32.7 R_0 \langle n_{e,20} \rangle (1 + s_n)}{\gamma_{CD} \langle T_{keV} \rangle (1 + s_t)} \right) \left[ \frac{MW}{m^3} \right] \tag{4.2}$$

where $\gamma_{CD}$ is the normalized current drive efficiency. This implies that:

$$f_{pcd} = \frac{S_{CD}}{S_{aux}} \tag{4.3}$$

where $f_{pcd}$ is the fraction of the applied heating power is needed to drive current. This calculation represents a divergence in the solutions of the model. If the solution with peak $Q_{fus}$ has $f_{pcd} \geq 1$, it suggests that this $Q_{fus}$ is not achievable without inductive current drive and that it is therefore not achievable by the NPGX.

To summarize, the physics model solves the power and ash particle balance for plasmas with combinations of density and temperature that have a $f_{\beta_{N,Max}} = 0.9$ and where $n_e \leq 0.85\ n_{gw}$ as defined by an input combination of ($R_0$, $A$, $B_0$, $q*/f_{bs}$). From this data, the combination of plasma density and temperature

with the maximum $Q_{fus}$ and $f_{pcd} \leq 1$ can be defined as the optimum operating point. As $Q_{fus}$ increases with $B_0$, the value of $B_0$ required to confine a plasma with $Q_{fus} \geq 2.5$ can be determined for a given combination ($R_0$, $A$, $q*/f_{bs}$) by iteration.

## 4.2 NBI Model

The NBI cost model described in section 2.3 requires that the particle energy of the neutral beam heating system(s) be calculated as it has a baring on whether cheaper PNBI can be used instead of NNBI. In the previous section, a distinction was made been 2 operating modes: either to run the NPGX with the maximum available plasma current whilst avoiding a kink instability ($q* = 3$) or to maximize the bootstrap fraction ($f_{bs} \rightarrow 100\%$). The later has the benefit that the external heating power is not required to drive current and therefore can be applied either tangential or perpendicular to the plasma surface. As perpendicular injection beams typically required lower beam energies to achieve the equivalent power deposition in the plasma center, operating an high bootstrap fraction could allow for a cost saving if the optimum operating point determined by the physics model allow that perpendicular PNBI systems be used for plasma heating instead of NNBI.

Therefore, the goal of the NBI model is to determine the energy of:

- a tangentially orientated beam capable of depositing a significant proportion of its beam power at the geometric center of the plasma and
- the maximum beam energy of a perpendicular neutral beam that can heat the plasma but does not significantly shine-through the plasma to heat the centerpost.

This was achieved by evaluating equation (3.23) along each beam lines shown in figure 4.3. To simplify the beam path geometry, it is assumed that the NBI travels on the tokamak's horizontal mid-plane (Z=0) and is aimed to intersect the plasma geometric center at its tangency point. It is also assumed that the energy of each beam particle is deposited on the flux surface on which the particle is ionized. The electron density variation along the beam line is calculated using equation (3.9) and requires a $\langle n_E \rangle$ and a density peaking factor be specified. For a perpendicular NBI system, the shine-through limit is set to 0.5% of the beam intensity.

As a benchmark for tangential NBI, the NBI model was applied to an ITER plasma. The results for varying beam energies are shown in figure 4.4. They imply that 32% of the beam energy of ITER's 1MeV beams is deposited inside the the normalized minor radius $\rho_{pc} = 0.2$. The beam energy of the NPGX's tangential NBI system will therefore be set to achieve the same level of beam penetration.

Based on the experiences of the ITER project, NBI systems with $>$ 1MeV beam energy would require significant time and expense to develop. It is therefore assumed that $1MeV$ is the maximum allowable beam energy.

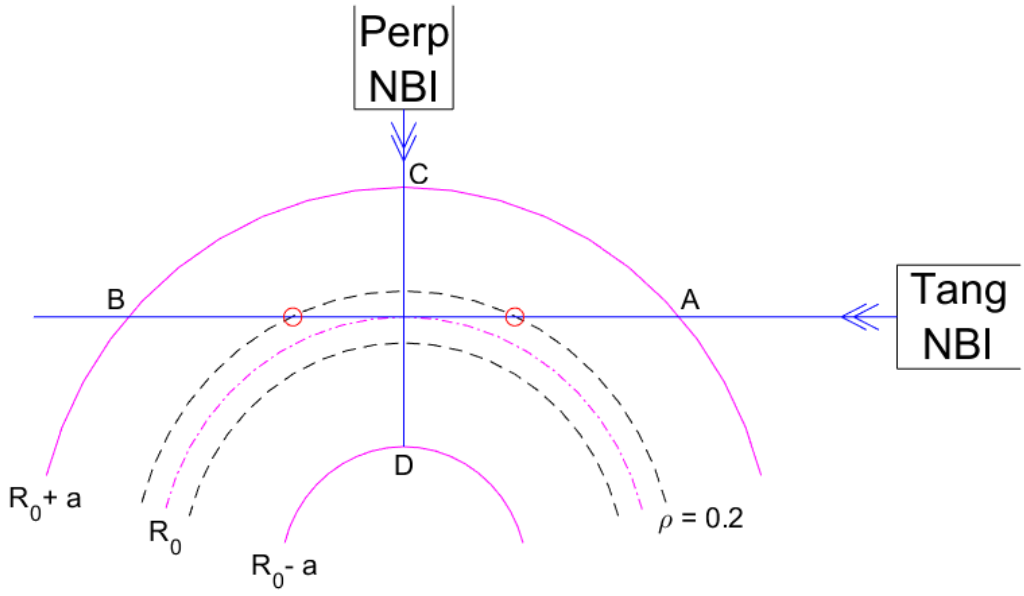


Figure 4.3: Schematic showing geometry for the tangential and perpendicular NBI model. For tangential injection (Tang NBI), neutral particles enter the plasma at point A (on Z=0 plane) and neutralize along the beam path (blue) before exiting at B. For perpendicular injection (Perp NBI), neutral particles enter the plasma at point C and leave at D. The beam energy is assumed to be deposited on the flux surface where the beam particle is ionized.

Table 4.2: List of Assumed Parameters for NBI Investigation

| **Parameter** | Symbol | **Value** | **Citation** |
|---|---|---|---|
| Tan. NBI Target Radius | - | $R_0$ | DC[1] |
| Boundary of Plasma Center | $\rho_{pc}$ | 0.2 | DC[1] |
| Perp. NBI Max Shinethrough | - | 0.5% | DC[1] |
| Max NBI Beam Energy | $E_{b,max}$ | 1000 | [45] |
| PNBI Energy Cut-off [keV/D] | - | 130 | [46] |

1: 'DC': Design Choice

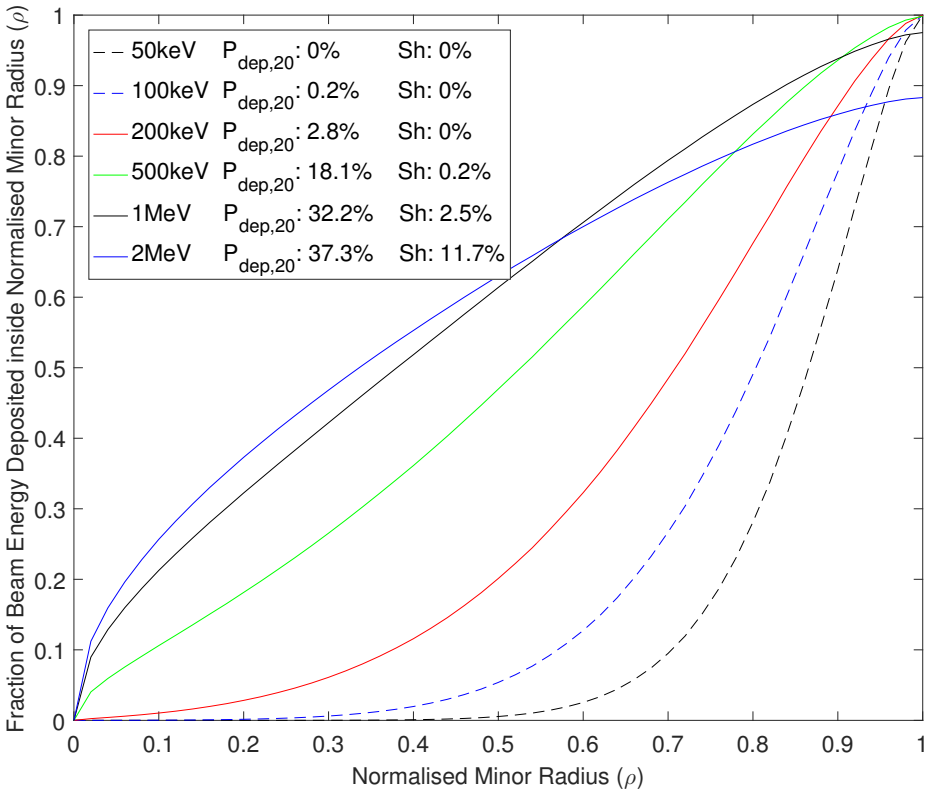


Figure 4.4: Fraction of NBI beam energy deposited inside the normalized minor radii for an ITER plasma ($R_0 = 6.2$, $A = 3$, $\langle n_e \rangle = 1\text{x}10^{20}$, $s_n = 0.5$) assuming tangential injection through the plasma's geometric center. As $E_{beam}$ increases, more of the beam energy penetrates to the plasma center. For a 1MeV beam, $\approx$32% of the beam energy is deposited inside $\rho = 0.2$.

## 4.3 Divertor Model

The goal of the Divertor model is to assess whether the heat flux from the plasma can be handled using only magnetic manipulation of the divertor plasma (in divertor parlance, this is referred to as an attached divertor plasma) or whether a significant amount of radiative cooling of the divertor plasma is required (a detached divertor plasma). This radiative cooling is typically initiated by actively fueling the divertor plasma to artificially raise its density. Avoiding the need for such a system would be advantageous as its inclusion would increase the complexity, and therefore the cost, of the NPGX. That said, the need for an active divertor fueling system may be unavoidable if physical sputtering of the divertor surface is found to be an issue, although sputtering is not investigated during this work. The model described below therefore only investigates whether divertor plasma detachment is required to manage the heat load on the divertor tiles.

The model is based on the work of Eich et al. [85] who developed a model for determining the divertor heat flux profile based on an outer mid-plane parallel heat flux[1] profile of $q_{||} = q_0 \exp(-\frac{r}{\lambda_q})$ for 'attached' divertor plasmas:

$$q_{||}(\bar{s}) = \frac{q_0}{2} \exp\left(\left(\frac{S}{2\lambda_q}\right)^2 - \frac{\bar{s}}{\lambda_q f_x}\right) . \operatorname{erfc}\left(\frac{S}{2\lambda_q} - \frac{\bar{s}}{S f_x}\right) + q_{BG} \tag{4.4}$$

where $\lambda_q$ is the integral power decay length at the outer mid-plane, $r = R_{sep} - R$, $R_{sep}$ is the major radius of the outer mid-plane LCFS, $q_{||}$ is the parallel heat flux impinging on the divertor surface (see figure 4.5), $q_0$ is the peak heat flux along the scrape-off layer at the outer mid-plane, $S$ is the power spreading factor, $\bar{s} = s - s_0$, $s_0$ is the radial distance of the strike point for the tokamak Z-axis, '$s$' is the distance away from $s_0$ along the divertor surface, $f_x$ is the effective flux expansion and $q_{BG}$ is the background heat flux to the divertor.

An example fit of equation (4.4) to experimental data taken from infra red thermography on a JET divertor tile is shown in see figure 4.5, right. The divertor heat load profile can be estimated using $q_{div} = q_{||}(\bar{s}) \cos\theta_{div}$ where $\theta_{div}$ is the angle between the direction of parallel heat flux and the divertor surface normal.

IR thermographic scans of divertor tiles on a number of tokamaks (including MAST and NSTX) were used to build a database of fits to experimental data [85]. This allowed scaling laws based on tokamak parameters to be determined for the unknowns $\lambda_q$ and $S$ [85, 101]:

$$\left(\frac{S_{[mm]}}{f_x}\right) = 0.12\ P_{LCFS[MW]}^{0.21}\ B_{p[T]}^{-0.82}\ R_{0[m]}^{0.71} \tag{4.5}$$

$$\lambda_q = 0.63\ B_{p[T]}^{-1.19} \tag{4.6}$$

where $P_{LCFS}$ is the power crossing the LCFS and $B_p = \frac{\mu_0 I_p}{L}$ is the poloidal magnetic field strength at the outer mid-plane[50] and $L$ is the perimeter length of the LCFS.

Using equation (4.4), equation (4.5) and equation (4.6) and assuming initial arbitrary values for $q_0$, a heat load profile for an 'attached' divertor plasma can

[1] the heat flux flowing parallel to the magnetic field lines

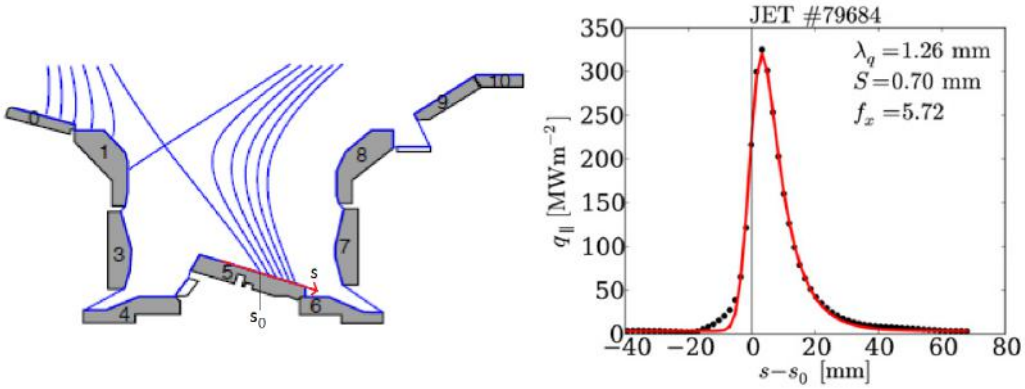


Figure 4.5: Example fit of divertor model to experimental data from JET. Left: Schematic of JET Scrap-off Layer showing flux lines and the theoretical strike surface used by equation (4.4) (Modified from [100]) Right: Example fit of equation (4.4) to data from JET plasma pulse 79684 [85].

Table 4.3: List of Assumed Parameters for Divertor Investigation

| **Parameter** | Symbol | **Value** | **Citation** |
|---|---|---|---|
| Divertor Strike Point | $s_0$ | $R_0 + a$ | DC[1] |
| Divertor Strike Point Angle | $\theta_{div}$ | 75° | DC[1] |
| Divertor Flux Expansion | $f_x$ | 20 | [102] |
| Max. Divertor Heat Flux $[MW/m^2]$ | $q_{max}$ | 10 | [45] |
| Divertor Surface Angle to Horizontal | - | 0° | DC[1] |

1: 'DC': Design Choice

be estimated based on plasma and tokamak parameters. This profile can then be integrated over the divertor surface, assuming a major radius for the divertor strike point ($s_0$), strike angle ($\theta_{div}$) and set flux expansion ($f_x$), to calculate the power impinging on the divertor ($P_{div}$). $q_0$ is adjusted until either $P_{div} \approx P_{LCFS}$ or the peak heat flux to the divertor surface ($q_{peak}$) is approximately equal to some predefined maximum ($q_{max}$). In the later case, the difference between the divertor heat load and LCFS power indicates the amount of the LCFS power that requires radiative dissipation. The resulting divertor radiative fraction ($f_{div}^{rad}$) is:

$$f_{div}^{rad} = \frac{(1 - P_{div})}{P_{LCFS}} \tag{4.7}$$

The need for radiative cooling would imply that a detached divertor plasma is required to manage heat loads. A list of characteristics and assumed values for the NPGX's divertor surface are shown in table 4.3.

## 4.4 Engineering Model

In this section, the engineering model is described, based on the engineering investigation described in section 3.2.

As was shown in section 3.2.4, an efficient TF coil should have the maximum number of of return limbs that it can accommodate. As having infinite limbs is impractical, the maximum number of TF return limbs available is limited to allow

access to the vacuum vessel. The largest external system that requires access to the vacuum vessel is for NBI heating. Based on the NNBI systems operating at JT60[103] and the LHD[104], the minimum distance allowed between TF limbs at the mid-plane is set to 1m.

Also shown in section 3.2.4 is that the TF limbs should be designed to have minimum self-inductance and that this can be achieved by maximizing their toroidal extent (referred to hereafter as the limb width ($w_{limb}$)) and minimizing their radial extent (referred to hereafter as the limb height ($h_{limb}$)). The geometrical problem is shown in figure 4.6. The centerpost is split into sections of angle $\Theta = 360/N_{limbs}$ wide. $w_{limb}$ is defined as 95% of the cord length of a section so as to not interfere will adjacent TF limbs: $w_{limb} = 2\ 0.95\ R_c \sin\frac{\Theta}{2}$ where $R_c$ is the radius of the centerpost ($R_c = R_0 - \frac{R_0}{A} - g$) and $g = 13.5$cm as defined in section 3.2.2.

$h_{limb}$ is optimized with respect to the mechanical requirements of the TF coil as radially thicker TF limbs would be stiffer, resulting in lower tension force transference to the centerpost, and would not heat up as quickly as each thicker limbs would be subject to a lower current density. The later implies that to ensure the limbs and centerpost heat up at the same rate during a pulse, the minimum total limb area should be equal to that of the centerpost:

$$N_{limbs}\ h_{limb,min}\ w_{limb} = A_{cp} \tag{4.8}$$

where $h_{limb,min}$ is the minimum limb height to achieve parity of these areas. However, the actual limb height is:

$$h_{limb} \quad = \quad h_x\ h_{limb,min} \tag{4.9}$$

where $h_x$ is the limb height multiplier. $h_x$ is set either to ensure a specified temperature rise in the limb or to avoid too high stresses in the TF coil system, which ever is larger.

To avoid the need for cooling channels to pass through the bulk material of the limb, a design choice was made to limit the temperature rise of the limb to $\approx$ 10K over the length of a pulse, compared to 100K for the centerpost. An analysis similar to that described in section 3.2.2 for the limb temperature rise was performed and compared to that for the centerpost (see figure 3.10, right). This comparison allowed a minimum $h_x = 2.55$ to be set to ensure this new restricted limb temperature rise.

The topology of the limb can be defined by sweeping the limb cross section along the CTC starting at $(R_s, Z_s)$. The location of $(R_s, Z_s)$ can be determined using the variables $w_{limb}$ and $h_{limb,min}$. The point on the limb cross-section about which the sweep occurs is positioned centrally on the limb section toroidally and at $(h_{limb,min}/2)$ in from the inside edge of the limb cross section in the poloidal plane. The resultant expression for $R_s$ is:

$$R_s = R_c \cos\frac{\Theta}{2} - \frac{h_{limb,min}}{2} \tag{4.10}$$

To define $(Z_s)$, the following needs to be defined:

1. The plasma shape

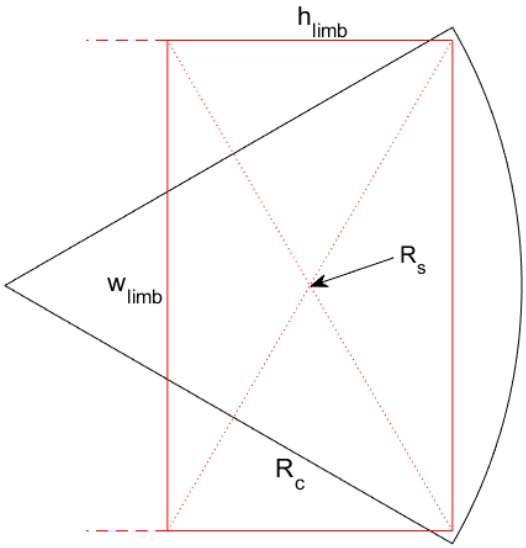


Figure 4.6: Plan view of Centrepost showing how the position of $R_s$ is determined for a example TF coil. The proposed limb area $A_{limb}$ is shown is red, the segment of the centerpost in black. Each has an equal cross sectional area. The red dashed line indicate the direction in which $h_{limb}$ can be extended to make $A_{limb} > A_c$ and for reinforcement purposes.

2. The height above the plasma of the inner divertor strike point surface
3. The shaping between the inner divertor strike point surface and
4. The size and shape of the Divertor coil

All but the last of these items can be determined using the plasma parameters ($R_0$, $A$). Using the calculated $I_p$ required to achieve $Q_{fus} = 2.5$ from the physics model, the current in the divertor coil is $I_{div} = I_p/3$. The area of the divertor coil can be calculated assuming the divertor coil's current density ($J_{div}$) is limited to ensure only a 10K temperature rise, similar to the TF limbs (ie. $J_{div} = J_{limb} = J_{rod}/h_x$).

A generic layout of the NPGX's poloidal cross section is shown in figure 4.7. To draw the TF coil, successive CTCs starting at $(R_s, Z_s)$ are drawn moving along the contour of equal 'C' until the inner side of the TF limb clears the Merging Compression chamber of the vacuum vessel. This chamber has a radial width of '$2a$' and contains the MC coils positioned at ($R_{MC} = R_0 + 2a$, $Z_{MC} = \kappa a$). The vacuum vessel walls at the top and bottom of the chamber is an arc of radius '$a$' and it is this wall that the TF coil's inside surface has to clear by a margin of 5cm.

The TF coil is completed by making the centerpost the same height as the maximum height of the TF limb and making the section of the centrepost above / below the two divertor coils an hourglass shape with a slope angle greater than that of the 'C' contour along which the CTC to extended. The TF limb's outer edge inside the radius of its maximum height is then altered so it meets the centerpost horizontally.

The other aspects of the tokamak poloidal cross section (Bv coil, Divertor layout, Shaping coils: Sh1, Sh2 and Sh3)) are then determined by the available space. Although they have been included for completeness, optimization of their

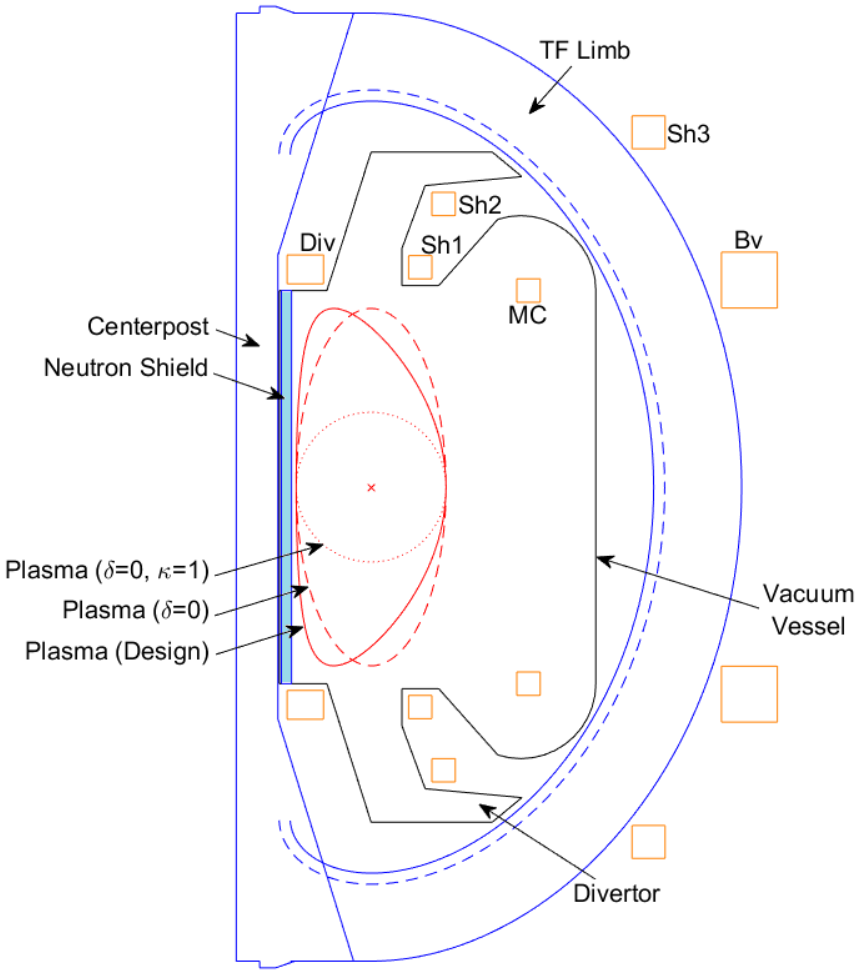


Figure 4.7: Generic Poloidal Cross Section of NPGX based on Engineering Model Design Algorithm.

Table 4.4: Relevant characteristics of the Maxwell model BMOD0165 P048 BXX super capacitor

| **BMOD165 P048 Bxx** | |
|---|---|
| Rated Capacitance ($C_{rated}$) | 165 F |
| Rated Voltage ($V_{rated}$) | 48 V |
| Projected Life | $10^6$ cycles |
| Capacitance Degradation over product life | 20% |

exact placement, size and shape would require an MHD equilibrium and was therefore deemed beyond the scope of this work.

The above results in 2 stage mechanical model. The first stage can be implemented alongside the physics model to determine the viability of a TF coil with respect to the heating of the centerpost. This viability can be tested by comparing the required current density to achieve $B_0$ ($J_{rod}$) is less that the limit to ensure $t_{pulse} \geq 25\tau_E$ or $\tau_{cr}$ set by figure 3.10, right. If the required current density exceeds this limit then the plasma configuration is not viable.

If the plasma configuration and associated TF coil are viable, the second stage of the analysis is to simulate the TF coil based on the inputs ($R_0$, $A$, $h_x \geq 2.55$) to test the coil's ability to achieve $B_0$ without exceeding the design stress limit. The TF coil topology model was implemented in MATLAB and the resulting dimensions were transferred to COMSOL, resulting in a full 3D model. COMSOL's Electromagnetics module was used to determine the resultant toroidal field from the applied coil current ($I_{coil} = I_{rod}/N_{limbs}$) and COMSOL's Structural Mechanics physics module was used to determine the TF coil's ability to withstand Lorentz forces with respect to the 250MPa design stress limit ($\sigma_{d,lim}$). The realism of the COMSOL model was benchmarked by comparing the predicted $B_0$ to that measured from the major radius of the COMSOL model. An example workflow is shown in figure 4.8.

Although a support structure for the TF coils will inevitably be included, it was found at this stage that the OFCu coil material itself provided sufficient strength to withstand the Lorentz forces. As a result the mechanical model is only constrained by a symmetry condition on the centerpost and is otherwise resting on the bottom surface of the centerpost.

## 4.5 Power Supply Model

Determination of $N_{SC}$ has been achieved using equation (3.30) to calculate $W_{bank}$ assuming the use of the Maxwell super capacitor model BMOD0165 P048 BXX. Based on this super capacitor's characteristics, which are shown in table 4.4, each super capacitor can store $\approx$ 150kJ of energy throughout their rated operating lives. Therefore:

$$N_{SC} = \frac{W_{bank}^{[J]}}{150000} \tag{4.11}$$

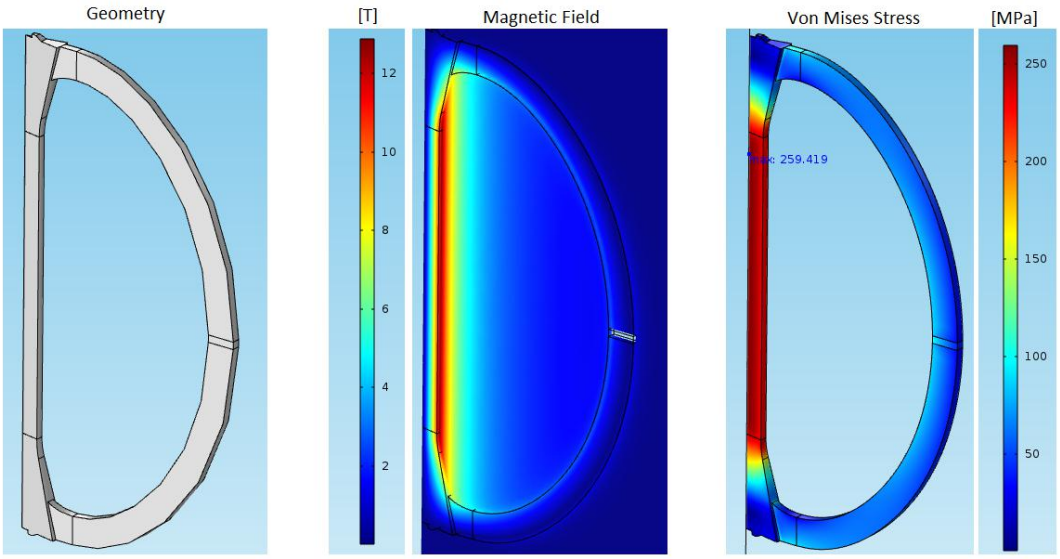


Figure 4.8: Workflow for a TF coil built by the engineering model around a plasma of $R_0 = 1$m and $A = 1.8$ (left) ($N_{limbs} = 16$, $h_X = 2.55$). When the coil is subjected to $I_{coil} \approx 1.42$[MA] a toroidal field of $B_0 = 4.51T$ (compared to $B_0 = 4.54T$ predicted) is produced (middle) with an initial centerpost temperature rise of 4.6[K/s]. The maximum von Mises stress is at on the axis of the centerpost: $\sigma_{VM,max} = 259.1$[MPa] which is greater than $\sigma_{d,lim}$ (right). This TF coil was deemed not capable of producing $B_0 = 4.51T$ without exceeding the design stress limit but, by reducing $I_{coil}$ by 2%, was capable of sustaining a $B_0 = 4.42T$ without exceeding $\sigma_{d,lim}$.

# 5. Results

In section 4, a number of models are defined that allow the physics and engineering of the NPGX tokamak to be analysed. In this section, these models are used in order to determine viable options. These options are then analysed in order to evaluate the most cost-effective NPGX experiment.

## 5.1 Plasma Model

In this section, the results of the plasma model - consisting of the physics, NBI, divertor and first stage mechanical models used concurrently - are presented. The goal of the plasma model is to determine the required $B_0$ for a plasma defined by $R_0$, $A$ and $f_{bs}$ and whether or not the tokamak adheres to operational limits. Repeated here for convenience, these limits are:

- $n_w \leq 4[\mathrm{MW}/m^2]$
- $E_{b,max} \leq 1\mathrm{MeV}$.
- $f_{rad}^{div} = 0\%$ and $q_{div} \leq 10[\mathrm{MW}/m^2]$
- $J_{rod}$ less than the limit to ensure $t_{pulse} \geq 25\tau_E$ $(= \tau_{pr})$
- $J_{rod}$ less than the limit to ensure $t_{pulse} \geq \tau_{cr}$

where $J_{rod} = 2\pi R_0 B_0/\mu_0 A_{cp}$ (see figure 3.10, right). The Plasma model was calculated for plasmas in the range $0.6 < R_0 < 1.5\mathrm{m}$ and $1.4 < A < 2$. An example result for a tokamak of $R_0 = 0.9\mathrm{m}$, $A = 1.8$ and $q^* = 3$ is shown in figure 5.1. The optimum operating point of this tokamak is marked on each subplot with an 'o'. This indicates that this tokamak can achieve $Q_{fus} = 2.5$ with $B_0 = 4.95\mathrm{T}$.

The results for the optimum operating point were determined for the full range of plasma shapes and sizes are shown in figure 5.2 and the space is partitioned with respect to the aforementioned operational limits. The figure shows that the most limiting restriction on the available plasma shapes and sizes, regardless of whether the plasma is operated with $q^* = 3$ or $f_{bs} = 90\%$, is the available centerpost current to achieve the required pulse length for partial current profile relaxation.

In section 4.2, the possibly of saving cost by using PNBI for plasma heating in conjunction with high bootstrap fraction plasmas was introduced. This is evaluated in figure 5.3 ($f_{bs} = 90\%$) which shows that the minimum beam energy in the available ($R_0$, $A$) space is 149KeV/D and, as this is more than the PNBI cut-off energy, implies that PNBI can not be used. Combining this with the finding that operating at high bootstrap fraction generally requires higher $B_0$ and $P_{aux}$ (see figure 5.4, right), implies that achieving $Q_{fus} = 2.5$ economically requires a tokamak operating at $q* = 3$. The available ($R_0$, $A$) space for an NPGX tokamak operating at maximum plasma current with contours of the $B_{0,req}$, $t_{pulse}$ and the volumetric cost indicator $P_{aux}$ is shown in figure 5.4, left.

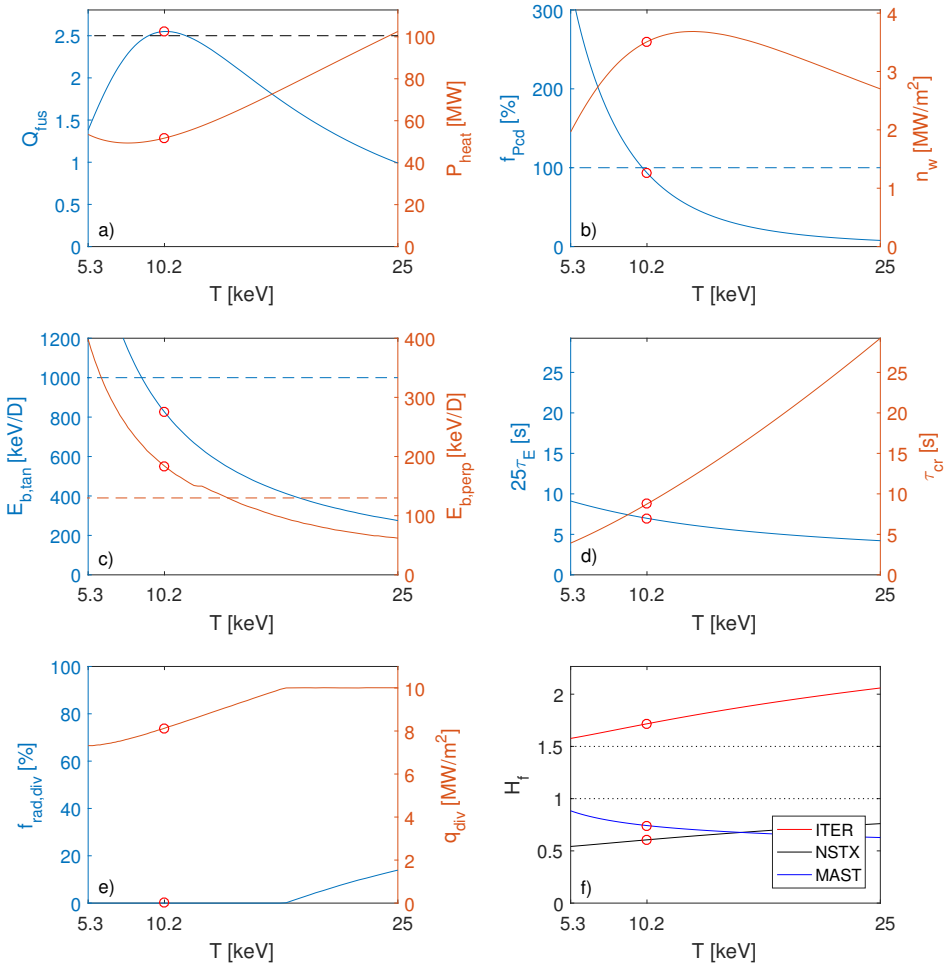


Figure 5.1: Results from Physics, NBI and Divertor Models for a Tokamak of ($R_0 = 0.9$m,$A = 1.8$, $B_0 = 4.95$[T], $q^* = 3$) using the PETTY energy confinement scaling with $H_f = 1.5$. The plots show a) $Q_{fus}$(left) and $P_{aux}$(right); b) $f_{pcd}$(left) and $n_w$(right); c) $E_{b,tan}$(left) and $E_{b,perp}$(right); d) $25\tau_E$(left) and $\tau_{cr}$(right); e) $f_{rad,div}$(left) and $q_{div}$(right) and f) the equivalent energy enhancement factors with respect to the ITER98(y,2), NSTX and MAST scalings. The optimum operating point was $\langle n_E \rangle \approx 4.25 \times 10^{20}/m^3$ and $\langle T \rangle = 10.2$keV. The operating point is marked on each subplot with a 'o'.

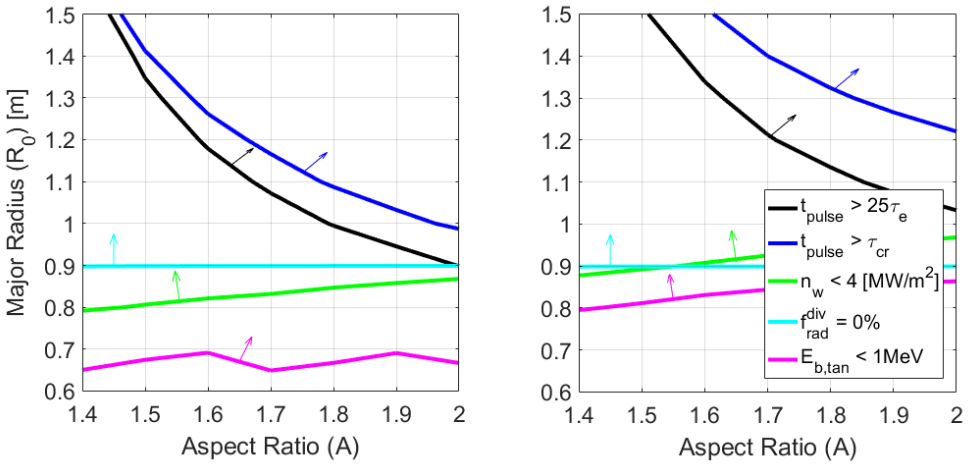


Figure 5.2: Output of the Plasma model with $q^* = 3$(left) and $f_{bs} = 90\%$(right) showing where in ($R_0$,$A$) space the limits of a) the available $I_{rod}$ to achieve $t_{pulse} = 25\tau_E$ without overheating equals that required to achieve $B_{0,req}$, b) the available $I_{rod}$ to achieve $t_{pulse} = \tau_{cr}$ without overheating equals that required to achieve $B_{0,req}$, c) the neutron wall loading ($n_w$) equals $4[MW/m^2]$, d) the NPGX can operate with attached divertor plasma and e) the limits on ($R_0$,$A$) for the NBI beam energy to be $<$ 1MeV. Arrows indicate side of limit line that is available operating space. In each case, the optimum operating point indicated by the Plasma model is taken.

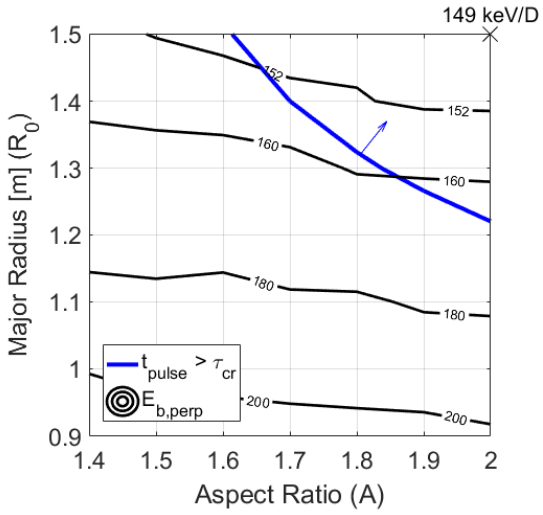


Figure 5.3: Output of Plasma model for $f_{bs} = 90\%$ showing the location in ($R_0$, $A$) space where the limit of $I_{rod}$ to achieve $t_{pulse} = \tau_{cr}$ without overheating equals that required to achieve the required $B_0$ to achieve $Q_{fus} = 2.5$ is overlaid with contours of the beam energy required to heat the plasma center without shine-through by the perpendicular NBI system.

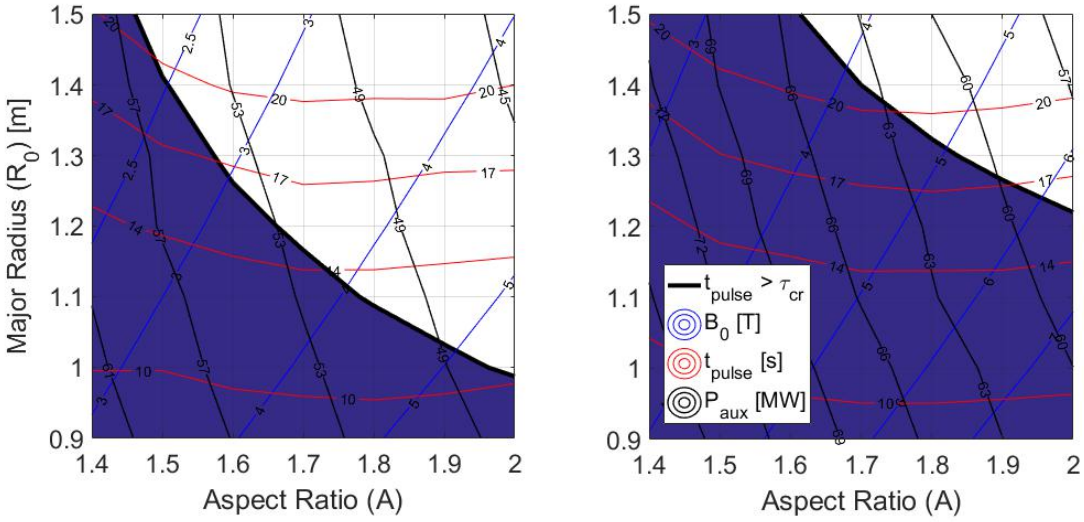


Figure 5.4: Output of Physics model with $q^* = 3$(left) and $f_{bs} = 90\%$(right) showing the magnetic field, pulse lengths and auxiliary heating power required to achieve a stable quasi-steady state plasma with $Q_{fus} = 2.5$. The area shaded blue is that excluded by the various limits depicted in figure 5.2.

## 5.2 Engineering Model

In this section, the output of the plasma model is fed into the mechanical model in order to define the approximate poloidal build of the remaining viable NPGX options and determine the required topology of the TF coil. As operating at high $f_{bs}$ has been shown not to result in a cost saving, this analysis only considers solutions with $q^* = 3$.

Figure 5.5 shows where in ($R_0$, $A$) space the TF coils that were analysed for this analysis were situated. An initial round of testing was performed using the minimum copper volume allowed by each coil ($h_x = 2.55$) and the results are shown in figure 5.6. This showed that a large proportion of the coils did not require $h_x$ to increase in order to provide the necessary toroidal field without breaking the design stress limit. Of those coils that did require stiffening, $h_x$ tended to increase rapidly, significantly increasing the cost of those TF coils and these candidate tokamaks were therefore excluded from consideration (blue boundary in figure 5.6).

Of the remaining coils, figure 5.6 also shows that the cost of each candidate tokamak increase roughly proportional to $R_0$. This implies that the minimum size tokamak that does not require extra stiffening of its TF limbs would be the most cost-effective solution for the NPGX. The most cost effective NPGX was therefore determined to be at ($R_0 = 1.13$[m], $A = 1.85$) and the physics and engineering parameters for this spherical tokamak are shown in table 5.1.

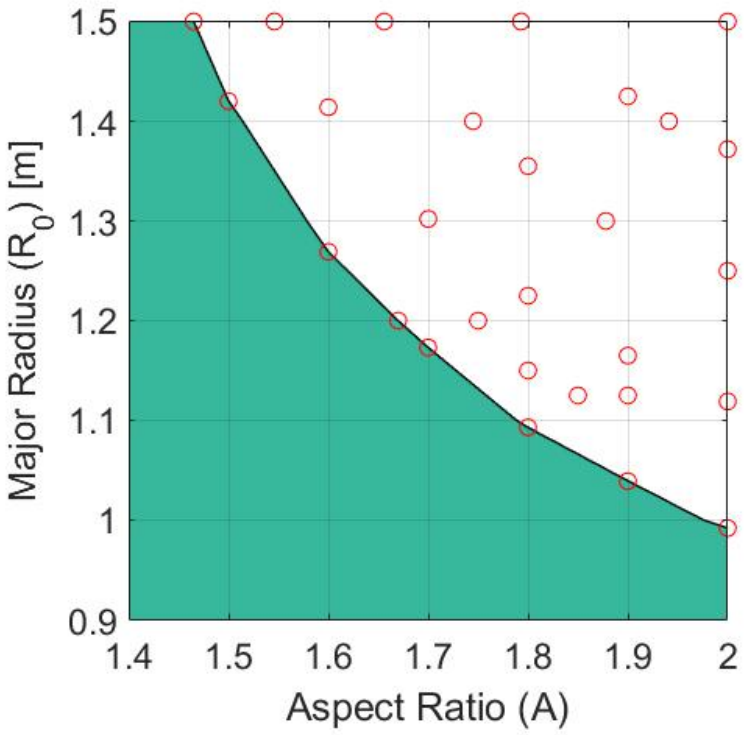


Figure 5.5: Output from Physics model with $q^* = 3$ used to determine which tokamaks should be studied using the mechanical model. The TF coils that were tested are denoted by a red 'o'.

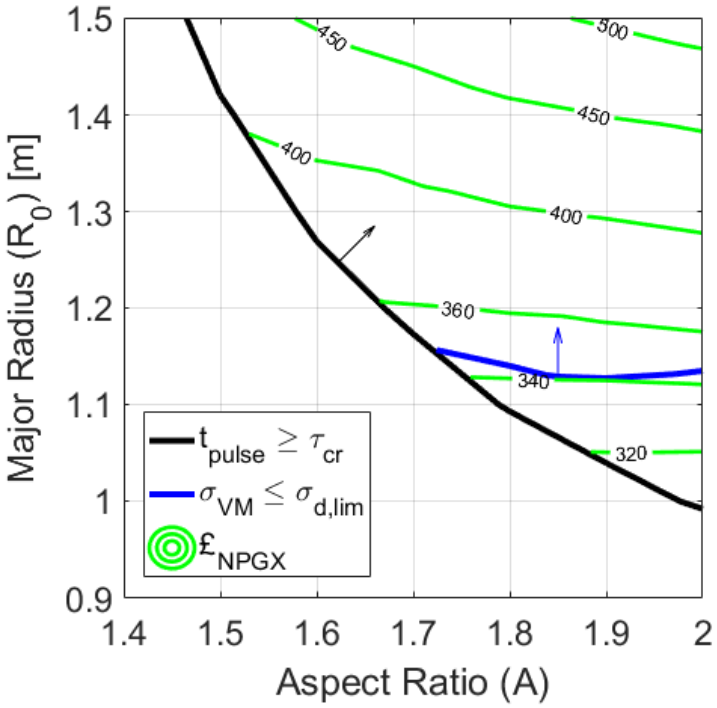


Figure 5.6: Output from Mechanical model ($q^* = 3$) showing the available ($R_0$, $A$) space from the physics model, overlaid with contours of NPGX costs (£m) and the limit of achieving $B_{0,req}$, both with the minimum TF coil copper volume ($h_x = 2.55$).

Table 5.1: Recommended NPGX Parameters

| | |
|---|---|
| $R_0^{[m]}$ / $A$ / $\kappa$ / $\delta$ | 1.13 / 1.85 / 2.35 / 0.5 |
| $V_p^{[m^3]}$ / $S_p^{[m^2]}$ | 18.8 / 45.8 |
| $B_0^{[T]}$ / $I_p^{[MA]}$ / $q^*$ | 4.35 / 7.8 / 3 |
| $\beta_t$ / $\beta_N$ | 12.8% / 4.41% |
| $Q_{fus}^{[MW]}$ / $P_{fus}^{[MW]}$ / $P_{aux}^{[MW]}$ | 2.55 / 125.1 / 49.1 |
| $f_{gw}$ / $\langle T \rangle^{[keV]}$ / $n_w^{[MW/m^2]}$ | 45% / 10.3 / 2.2 |
| $f_{He}$ / $\langle p \rangle^{[atm]}$ / $\langle p\tau_E \rangle^{[atms]}$ | 1.52% / 9.5 / 3.69 |
| $E_{b,tan}^{[keV/D]}$ / $Sh_{b,tan}$ | 705 / 2.93% |
| $f_{rad}^{div}$ / $q_{div}^{[MW/m^2]}$ | 0% / 4.65 |
| $f_{bs}/f_{pcd}$ | 56.4% / 88% |
| $\tau_e^{[s]}$ / $\tau_{pr}^{[s]}$ / $\tau_{cr}^{[s]}$ | 0.388 / 9.7 / 13.74 |
| $H_{PETTY}$ / $H_{ITER}$ | 1.50 / 1.74 |
| $H_{NSTX}$ / $H_{MAST}$ | 0.70 / 0.77 |
| $J_{rod}^{[MA/m^2]}$ / $N_{limbs}$ | 53.0 / 18 |
| $L_{coil}^{[\mu H]}$ / $R_{coil}^{[\mu\Omega]}$ | 12.9 / 0.76 |
| £$_{tok}$ / £$_{aux}$ / £$_{ps}$ | 95m / 221m / 25m |
| £$_{NPGX}$ [1] / £$_{TOTAL}$ [2] | 341m / 1.08bn |

[1] £$_{NPGX}$ is the cost of just the NPGX device

[2] £$_{TOTAL}$ is the cost of NPGX device, buildings and auxiliary equipment

# 6. Summary and Conclusion

One potential solution for providing near-carbon-neutral electricity production is to build reactors that utilize the deuterium-tritium thermonuclear fusion reaction. To be economical, these reactors need to output sufficient electrical power to cover the recirculating power requirements of the reactor, with enough left over to sell at an affordable price. Large strides have been made since the 1950s to determine the best way to build such a reactor but further experimentation is still required. Based on a review of currently operating and planned fusion experiments, it was determined that a spherical tokamak that could achieve $Q \geq 2.5$, designated herein as the 'Net Power Gain Experiment' (NPGX), could prove a worthwhile additional experiment as long as it was cost-effective.

This work sought to determine what capital expenditure would be required to build the NPGX to achieve $Q \geq 2.5$. An investigation was undertaken to determine a method of estimating the cost of the NPGX based on the parameters of its components and a simple cost model was defined. In order to assign values to the parameters, a literature search into the physics and engineering associated with spherical tokamak design was undertaken. This knowledge was used to build models to account for the NPGX's critical characteristics and, with the exception of the divertor model, all formulae utilized have been used by other TDAs for a similar purpose. These models were used to determine viable NPGX design options and their associated capital cost.

A range of shapes and sizes of spherical tokamaks were tested ($0.6 < R_0 < 1.5$m, $1.4 < A < 2$) and the analysis implied that the most cost-effective NPGX spherical tokamak should have $R_0 = 1.13$m, $A = 1.85$ and $B_0 = 4.35T$ and could output $P_{fus} = 125$MW and achieve $Q = 2.55$. Other parameters associated with this solution are shown in table 5.1. This NPGX has a capital roughly £1.08bn, an estimate similar to that expended on the JET tokamak to reach $Q = 0.55$. This work also suggests that, compared to JET, the NPGX would generate more fusion power at this higher fusion power gain and over timescales sufficient to achieve near pressure profile equilibrium and partial current profile equilibrium.

Although care was taken to ensure sufficient accuracy whilst accounting for as many aspects of tokamak design as possible, this analysis can only be considered an introductory study. In comparison to this study, other tokamak concepts are better developed and the specialist tools used to define them (TDAs) more complex as they account for more of the relevant physics. There are areas where improvements could be made and some ideas of how to achieve this are detailed in section 7.

That said, the goal of this design study was to determine what capital expenditure would be required to build an ST with $Q \geq 2.5$ whilst using currently available materials and presently accepted understanding of energy confinement in fusion plasmas. It has concluded on a tokamak that, given the size and shape of current, planned and proposed tokamak experiments described in the literature, is not outside the realms of possibility and with a price tag within the range of what was expected. Subject to the further work detailed in section 7 being undertaken, the next step would be to perform a more detailed design study based on a spherical tokamak with $R_0 = 1.13$m and $A = 1.85$ in order to benchmark the

models described in this work and update the design recommendation if required. This work would also require updating based on the results from STs experiments due to start experimenting in the next few years (ST40, MAST-U and NSTX-U).

# 7. Suggested Further Work

A number of areas have been identified that should be investigated before moving onto a more detailed design study. These include:

- *Increase scope and accuracy of cost model.* For much the same reasons that the initial ITER costs published in 1999 [36] did not reflect the true cost of the ITER project, the cost model described in section 2 could be improved upon to increase both its breath and accuracy if a more detailed breakdown of the costs for each component of the ITER project for 2008 became publicly available (on which [39] is based). This would allow more accurate estimates for of the single biggest cost associated with any present-day fusion experiments (the construction of a building in which to house the experiment and its associated equipment) whilst accounting for fluctuations in commodity prices. There are also costs associated with running the experiment and the licensing of nuclear sites which are not included in the NPGX cost model. The ARIES team are making an effort to document and update their cost databases and tokamak costing algorithms to reflect current data [37] and, when published, that data would prove invaluable in improving the NPGX cost model.

- *Improve design of neutron shielding.* During this project, detailed analysis of how neutrons interact with solid matter was not used although attempts were made to utilize the open source software GEANT4 [105] for this purpose. As a result, the neutron shielding of the NPGX was not designed with reference to MCNP simulation, as was desired, but less rigorously. MCNP would have allowed more effects of neutron bombardment, especially in the area of the NPGX's centerpost, to be studied. These could include any concentrated heating caused by the NPGX's geometry, heating of the centerpost due to the secondary emission of gamma rays and an assessment of the chemical changes that could occur in the centerpost and moderator material. Each of these areas is covered during the design of other tokamak concepts [92] and is likely to effect the design and performance of the NPGX.

- *Add complexity to the description of the plasma.* During the literature search into the plasma model described in section 3.1, data was drawn from a large number of Tokamak Design Algorithms (TDAs). Compared to these TDAs, the plasma model described herein is a simplicity approach and therefore could be extended to account for more complex plasma features. Examples include that 1) a 2D plasma profile could implemented based on, for example, a Soloviev Equilibrium [106] and 2) that the plasma's density and temperature profiles should be assigned a non-zero value at the LCFS and a value at the top of the edge pedestal characteristic of operating in H-mode.

- *Including an assembly procedure as part of the design.* Tokamak assembly considerations were not included in this project due to time constraints but many other tokamaks include assembly considerations as part of there conceptual design phase [33, 92]. Designing a tokamak for ease of assemble

is a key design feature of useful experiments as it goes hand-in-hand with ease of maintenance and having a tokamak that is easy to maintain increases the chances that it would be successful.

- *Include a model for the optimized design of either the merging compression system or an alternative.* During the mechanical model it was noted that one of the key limiting factors affecting the size of the TF coil is the placement of the merging compression coils. In this work, design choices were made that defined the MC coil's placement resulting in a large proportion of the vacuum vessel being under utilized. On reflection, a more detailed model for the placement of the MC coils may (or may not) result in them being moved to a location that would allow the TF limbs to be reduced in size, reduce the size of the unused part of the vacuum vessel and the overall cost of the NPGX's tokamak core. Alternatively, other plasma initiation systems such as double-null merging or systems that use electron-beinstein waves [107] could be used.

# 8. Acknowledgements

Special thanks also go to Mr. Alan Sykes (TE) and Prof. Niek Lopes Cardozo (TU/e) whose supervision and patient guidance always smoothed the way for progress.

Many thanks go out to all the staff at Tokamak Energy for their help and support during this work. Particularly thanks go to Mikhail Gryaznevich, Alan Costley, Colin Windsor, Peter Buxton, Otto Asunta, Graham Dunbar, Bill Huang, Tony Langtry and Adrian MacFarland.

# Bibliography


[1] United Nations Department of Economic and Social Affairs, Population Division. "World population to 2300". `http://www.un.org/esa/population/publications/longrange2/WorldPop2300final.pdf`, 2004. [Online; access 03-Mar-2016].

[2] World bank open database. `http://data.worldbank.org/`, 2015. [Online; accessed 03-Mar-2016].

[3] United Nations. "Kyoto Protocol to the United Nations Framework: Convention on Climate Change". `http://unfccc.int/resource/docs/convkp/kpeng.pdf`, 1998. [Online; accessed 10-May-2016].

[4] Roisin Quinn. Future energy scenarios 2015. *UK National Grid*, March 2015.

[5] International Energy Agency. World Energy Outlook 2014 - Executive Summary. `www.iaea.org`, 2014. [Online; accessed 04-Mar-2016].

[6] International Energy Agency. Key World Energy Statistics. `www.iaea.org`, 2014. [Online; accessed 04-Mar-2016].

[7] Li et al. "A new simple formula for fusion cross-sections of light nuclei". *Nucl. Fus*, 48, 2008.

[8] I. Hore-Lacy. *"Nuclear Energy in the* $21^{st}$ *Century"*. World Nuclear University Press, $3^{rd}$ edition, 2012.

[9] J. Freidberg. *"Plasma Physics and Fusion Energy"*. Cambridge University Press, $1^{st}$ edition, 2007.

[10] D. Clery. *"A Piece of the Sun - The Quest for Fusion Energy"*. Overlook Duckworth, $1^{st}$ edition, 2013.

[11] Lawson J.D. "Some Criteria for a Power Producing Thermonuclear Reactor". *Proc. Physics Society*, B70, 1954.

[12] L. A. Artsimovich. "Tokamak Devices". *Nuclear Fusion*, 12, 1972.

[13] EFDA. "EUROfusion Website". `www.euro-fusion.org`, 2012. [Online; accessed 17-Mar-2016].

[14] Keilhacker et al. "High fusion performance from deuterium-tritium plasmas in JET". *Nuclear Fusion*, 39, 1997.

[15] L. Horton et al. "JET experiments with tritium and deuterium–tritium mixtures". *Fusion Eng. Des.*, 109-111, 2016.

[16] Gryaznevich et al. "Achievement of record beta in the START spherical tokamak.". *Physic Review Letters*, 80, 1998.

[17] N.H. Balshaw. "Comparison Table of Spherical Tokamaks". http://www.tokamak.info/, September 2015.

[18] R. D. Stamburgh et al. "The Spherical Tokamak Path to Fusion Power". *Fusion Technology*, 33, January 1998.

[19] H. R. Wilson et al. "The Spherical Tokamak Fusion Power Plant". *IAEA*, 1997.

[20] Najmabadi et al. "Spherical torus concept as power plants/the ARIES-ST study". *Fusion Engineering Design*, 65, 2003.

[21] G. M. Voss et al. "Development of the spherical tokamak power plant". *Fusion Eng. Des.*, 63-64:65–71, 2002.

[22] A. Sykes et al. "Recent Advances on the Spherical Tokamak Route to Fusion Power". *IEEE Transactions on Plasma Scienec*, 42, 2014. doi: 10.1109/TPS.2014.2304569.

[23] EFDA. "Fusion Electricity - A roadmap to the realisation of fusion energy". www.euro-fusion.org, 2012. [Online; accessed 17-Mar-2016].

[24] ITER Physics Expert Groups on Confinement and Transport and Confinement Modeling and Database. "Chapter 2: Plasma confinement and transport.". *Nucl. Fusion*, 39, 1999.

[25] C. Bachmann et al. "Initial DEMO tokamak design configuration studies". *Fusion Engineering and Design*, 98-99, 2015.

[26] B. Sorbom et al. Arc: A compact, high-field, fusion nuclear science facility and demonstration power plant with demountable magnets. *Fusion Energy and Design*, 100:378–405, 2015.

[27] B. Mumgaard et al. SPARC - Soonest/Smallest Private-Funded Affordable Robust Compact. https://www.youtube.com/watch?v=fKREB8IvCbs, 2016. [Online; accessed 21-Mar-2016].

[28] T. Brown et al. "PPPL ST-FNSF Engineering Design Details". *Fusion Science and Technology*, 68, September 2015. doi: 10.13182/FST14-911.

[29] CCFE. "Culham Centre for Fusion Energy Website". www.ccfe.ac.uk, 2012. [Online; accessed 28-Oct-2016].

[30] PPPL. "Princeton Plasma Physics Laboratory Website". www.pppl.gov, 2016. [Online; accessed 28-Oct-2016].

[31] Faster Fusion Leaflet. http://www.tokamakenergy.co.uk/, 2016. [Online; accessed 21-Mar-2016].

[32] M. Ono et al. "Making of the NSTX Facility". *18th Fusion energy Conference, Sorrento, Italy 4-10 Oct*, 2000.

[33] Menard et al. "Fusion nuclear science facilities and pilot plants based on the spherical tokamak.". *Nuclear Fusion*, 56, 2016.

[34] Mathworks - the makers of matlab and simulink. http://uk.mathworks.com/, 2016. [Online; accessed 12-Aug-2016].

[35] COMSOL - multiphysics modeling software. https://www.comsol.com/, 2016. [Online; accessed 12-Aug-2016].

[36] ITER Engineering Design Activities. "Technical Basis for the ITER Final Design Report, Cost Review and Safety Analysis". *IAEA, Vienna*, 1998.

[37] Dragojlovic et al. "ARIES: An Advanced computational algorithm for systems analysis of tokamak power plants". *Fusion Eng. Des.*, 85, 2010.

[38] ITER Engineering Design Activities. "Summary of the ITER Final Design Report". *IAEA, Vienna*, 2001.

[39] ITER Engineering Design Activities. "Status of the ITER Project". *European Commission*, 2010.

[40] "Historical Exchange Rates from 1953 with graphs and charts". http://fxtop.com/en/historical-exchange-rates.php, 2016. [Online; accessed 13-Feb-2017].

[41] "Historical UK inflation rates and calculator". http://inflation.stephenmorley.org/, 2017. [Online; accessed 13-Feb-2017].

[42] M. Glugla et al. "The ITER tritium systems". *Fusion Engineering and Design*, 82, 2007.

[43] H. Weison et al. "The Scientific Case for a JET D-T Experiment EFDA–JET–CP(13)04/06". 2013. [Online; accessed 13-Feb-2017].

[44] M. Ni et al. "Tritium supply assessment for ITER and DEMOnstration power plant". *Fusion Engineering and Design*, 88, 2013.

[45] Doyle et al. "Chapter 2: Plasma confinement and transport.". *Nucl. Fusion*, 47, 2007.

[46] Beckner et al. "Intense, mixed-energy hydrogen beams for CTR injection". *Nucl. Fusion*, 15, 1975.

[47] Ciric et al. "Overview of the JET neutral beam enhancement project". *Fusion Eng Design*, 82, 2007.

[48] Toigo et al. "Progress in the realization of the PRIMA neutral beam test facility". *Nucl. Fusion*, 55, 2015. doi: 10.1088/0029-5515/55/8/083025.

[49] Kovari et al. "PROCESS: a systems code for fusion power plants - Part 1: Physics". *Fusion Engineering and Design*, 89, 2015.

[50] Johner J. "HELIOS: A zero-dimensional tool for next step and reactor studies". *Fusion Sci. Tech.*, 59, 2010.

[51] A. Costley et al. "On the Power and Size of Tokamak Fusion Pilot Plants and Reactors". *Nucl. Fus.*, 5, 2015.

[52] Petty C.C. et al. "Sizing up plasmas using dimensionless parameters". *Physics of Plasmas*, 15, 2008.

[53] "The International H-Mode Confinement Database Version DB3v13f (and DB3v13)". `http://efdasql.ipp.mpg.de/HmodePublic/DataDocumentation/Datainfo/DB3v13/db3v13.htm`, 2016. [Online; accessed 28-Nov-2016].

[54] Alan Sykes. "The Spherical Tokamak Programme at Culham". *17th IAEA Fusion Energy Conference*, October 1998.

[55] Valovic M. et al. "Scaling of H-mode energy confinement with $I_p$ and $B_t$ in the MAST spherical tokamak". *Nucl. Fusion*, 49, 2009. doi: 10.1088/0029-5155/49/7/075016.

[56] Kaye S. M. et al. "Energy Confinement Scaling in low aspect ratio NSTX tokamak.". *Nucl. Fusion*, 47, 2006. doi: 10.1088/0029-5155/46/10/002.

[57] L.E. Zakharov. "LiWall Fusion - The New Concept of Magnetic Fusion". *PPPL-4595*, 2011. doi: /10.2172/1001686.

[58] G. Z. Zuo et al. "First results of lithium experiments on EAST and HT-7". *Journal of Nuclear Materials*, 415, August 2011.

[59] D. N. Ruzic et al. "The effect of lithium wall conditioning in TFTR on plasma surface interactions". *Journal of Nuclear Materials*, 266-269, 1999.

[60] Majeski et al. "Enhanced Energy Confinement and Performance in a Low-Recycling Tokamak". *Physics Review Letters*, 97, 2006.

[61] V. A. Evitikhin et al. "Technological aspects of lithium capillary-pore systems application in tokamak device". *Fusion Engineering and Design*, 56-57, 2001.

[62] Kessel et al. "Plasma profile and shape optimization for the advanced tokamak power plant, ARIES-AT". *Fusion Engineering and Design*, 80.1-4, 2005. doi: /10.1016/j.fusengdes.2005.06.350.

[63] Gates et al. "Plasma control on the National Spherical Torus Experiment". `https://www.lehigh.edu/~eus204/workshop/fcw/talks/Gates_talk.pdf`, 2016. [Online; accessed 08-Dec-2016].

[64] Miller et al. "Non-circular, finite aspect ratio, local equilibrium model". *Plasma Physics*, 1998. doi: 10.1088/1.872666.

[65] Becker et al. "Empirical scaling laws for local transport in neutral beam heated plasmas.". *Nucl. Fus*, 28, 1994.

[66] Hillis et al. "Helium exhaust and transport studies with the ALT-II pump limiter in the TEXTOR tokamak.". *Phys. Rev. Letters*, 65, 1990.

[67] Jakobs et al. "Fusion burn equilibria sensitive to the ratio between energy and helium transport". *Nuclear Fusion*, 54, 2014.

[68] D. Meade. "Fusion Ignition Research Experiment (FIRE)". `http://fire.pppl.gov/Snowmass_BP/FIRE.pdf`, 2002. [Online; accessed 13-Feb-2017].

[69] D.R. Mikkelsen. "Current relaxation time scales in toroidal plasmas". *Physics of Fluids B*, 1, 1988. doi: 10.1063/1.859146.

[70] F. Troyon et al. "MHD-limits to Plasma Confinement". *Plasma Physics and Controlled Fusion*, 26(1A):209–215, 1984.

[71] Peng et al. "A component test facility based on the spherical tokamak". *Plasma Physics and Controlled Fusion*, 47, 2005. doi: 10.1088/0741-3335/47/12B/S20.

[72] Greenwald et al. "A new look at density limits in tokamaks". *Nuclear Fusion*, 28, 1988.

[73] Gates et al. "Origin of Tokamak Density Limit Scalings". *Physics Review Letters*, 108, 2012.

[74] T. Hender. "Spherical tokamak power plant design issues". *Fusion Engineering and Design*, 48, 2000.

[75] Galeev et al. "Transport Phenomena in a Collisionless Plasma in a toroidal magnetic system". *Soviet Physics JETP*, 23, 1968.

[76] Bickerton et al. "Diffusion Driven Plasma Currents and Bootstrap Tokamak". *Nature Physical Science*, 229, 1971.

[77] Zarnstorff et al. "Bootstrap Current in TFTR". *Physics Review Letter*, 60, 1988.

[78] Coda et al. "Steady-state, fully bootstrap-sustained discharge in the TCV tokamak". 2006.

[79] Andrade et al. "Scaling of bootstrap current on equilibrium and plasma profile parameters in tokamak plasmas". *Plasma Phys. Control. Fusion*, 50, 2008.

[80] ITPA Confinement and H-mode Threshold Database Working Group (snipes J.A.). "Multi-Machine Global Confinement and H-mode Threshold Analysis". *Proc of 19th IAEA Int Conf on fusion Energy, Lyon, France 14-19 October 2002*, CT/P-04, 2002.

[81] Takizuka T. el al. "Roles of aspect ratio, absolute B and effective Z of the H-mode power threshold in tokamaks of the ITPA database". *Plasma Phys. Control. Fusion*, 46, 2004. doi: 10.1088/0741-3335/46/5A/024.

[82] Martin Y.R. et al. "Power requirement for accessing the H-mode in ITER". *11th IAEA Technical Meeting on H-mode Physics and Transport Barriers*, 123, 2008.

[83] Ryter F. and H-mode Threshold Database Group. "Progress of the international H-mode power threshold database activity". *Plasma Phys. Control. Fusion*, 44, 2002.

[84] Petty C. C. et al. "Feasibility Study of a Compact Ignition Tokamak Based on the GryoBohm Scaling". *Fusion Technology*, 43, 2002.

[85] Eich et al. "Scaling of the tokamak near the scrape-off layer H-mode power width and implications for ITER". *Nuclear Fusion*, 53, 2013. doi: 10.1088/0029-5515/53/9/093031.

[86] A. Salmi et al. "Neutral beam optimisation for the spherical tokamak ST40". *Fusion Engineering and Design*, 117, 2017.

[87] A.C. Rivere. "Penetration of fast hydrogen atoms into a fusion reactor plasma". *Nuclear Fusion*, 11, 1971.

[88] D.R. Sweetman. "Ignition condition in tokamak experiments and role of neutral injection heating". *Nuclear Fusion*, 13, 1973.

[89] Simon N.J. et al. "NIST Monograph 177: Properties of Copper and Copper Alloys at Cryogenic Temperature". *National Institute of Standards and Technology*, 177, 1992.

[90] Copper Development Associations. "Copper Mechanical Properties". `http://copperalliance.org.uk/`, November 2016.

[91] T. Hayashi. "Neutronics assessment of advanced shield materials using metal hydride and borohydride for fusion reactors". *Fusion Engineering and Design*, 81, 2006.

[92] G.M. Voss et al. "Conceptual design of a component test facility based on the spherical tokamak". *Fusion Eng. Des.*, 83, 2008.

[93] S. M. A Kazini. *"Solid Mechanics"*. Tata McGraw-Hill Publishing, $1^{st}$ revised edition, 2006.

[94] D. Griffiths. *"Introduction to Electrodynamics"*. Pearson Education Limited, $4^{th}$ edition, 2007.

[95] "HTS – An Enabling Technology for Spherical Tokamak Fusion Reactors". `https://www.stfc.ac.uk/files/uk-magnetics-tokamak-energy/`, 2015. [Online; accessed 15-Feb-2017].

[96] Sykes et al. "Plasma current formation in MAST without use of central solenoid". *32nd EPS Conference of Plasma Physics*, 29C, 2005.

[97] Sips et al. "Assessment of the Baseline Scenario at q95=3 for ITER". *IAEA Conference 2016*, EX/P6-42, 2016.

[98] Gryaznevich et al. "Fast particles in a steady state compact FNS and compact ST reactor". *Nuclear Fusion*, 54, 2014. doi: /10.1088/0029-5515/54/10/104005.

[99] Gormezano et al. "Progress in the ITER Physics Basis Chapter 6: Steady State Operation". *Nuclear Fusion*, 47, 2007. doi: /10.1088/0029-5515/47/6/S06.

[100] G. Arnoux et al. "Plasma-wall heat loads in ITER-like advanced Tokamak scenarios on JET". *34th EPS Conference on Plasma Physics*, 31F, 2007.

[101] Eich et al. "Scaling of the divertor power spreading (S-factor) in open and closed divertor operation in JET and ASDEX Upgrade". *Nuclear Materials*, 463, 2015. doi: 10.1016/j.jnucmat.2014.11.076.

[102] Havlickova et al. "SOLPS analysis of the MAST-U divertor with the effect of heating power and pumping on the access to detachment in the Super-x configuration". *Plasma Phys. Control. Fusion*, 57, 2015.

[103] Itoh et al. "Beam performance of negative-ion based NBI system for JT-60". *Fusion Eng and Design*, 51-52, 2000.

[104] Takeiri et al. "High-power and long-pulse injection with negative-ion-based neutral beam injectors in the Large Helical Device". *Nucl. Fusion*, 46, 2006.

[105] J. Allision et al. . "Geant4 a simulation toolkit". *Nuclear Instruments and Methods in Physics Research A*, 506, 2003.

[106] J.P. Goedbloed, R. Keppens, S. Poedts. *"Advanced Magnetohydrodynamics"*. Cambridge University Press, $1^{st}$ edition, 2010.

[107] R. Raman and V. F. Shevchenko. Solenoid-free plasma start-up in spherical tokamaks. *Plasma Physics Control Fusion*, 56(19pp):103001, September 2014.

# A. World Electricity Demand Calculation for 2050

Carbon-neutral energy sources are increasing becoming an integral part of the energy landscape but there share of the world's total energy supply is unlikely to rise above 25% by 2050 [5]. This leaves the remaining 75% to be provided by other energy sources, including fossil fuels. The current world energy supply is about 13.5 Gtoe per year[1] ($\approx 5.7 \times 10^{20}$J per year), 18% of which is in the form of electricity[6].

For all energy sources, this is equivalent to a continuous use rate of 18TW (3.2TW as electricity) and, based on the prediction that global energy consumption will rise by 300%, will rise to 72TW by 2050. Removing the fraction to be provided by renewable technologies (25%) and assuming that electricity use makes up 40% of the remainder (increased from 18% due to electrification of transport and domestic heating), worldwide demand for electricity could rise from 3.2 to 21.6TW in 2050 based on a continuous use rate.

[1]Gtoe - gigaton of Oil equivalent. 1 Gtoe $\approx 4.2 \times 10^{19}$ Joules, data for 2013

# B. Formulae used to calculate Power Balance terms.

**Alpha Particle Heating** [9]

$$S_\alpha = n_d n_t \langle \sigma v \rangle E_\alpha \tag{B.1}$$

**Ohm Heating by Inductively Drive Plasma Current** [51]

$$S_\Omega = \frac{1}{V_p} \frac{5.6 \times 10^4}{1 - 1.31\epsilon^{0.5} + \epsilon} \frac{R_0 I_p}{a^2 \kappa T_{keV}^{1.5}} \tag{B.2}$$

**Bremsstrahlung Radiation** [67]

$$S_{brems} = 5.35 \times 10^{-37} \frac{2\sqrt{3}}{\pi} T_{keV}^{0.5} n_e^2 Z_{eff} \tag{B.3}$$

**Line Radiation** [9]

$$S_{line} = \frac{1}{V_p} \int_{V_p} \sum_i n_e n_i L_i \, dV_p \tag{B.4}$$

**Cyclotron Radiation** [51]

$$S_{cyclo} = \frac{0.414}{V_p} n_{e,20}^{0.5} T_{kev}^{2.5} B_0^{2.5} \sqrt{1 - R_f} \, (a\sqrt{\kappa})^{-0.5} \, (1 + 2.5 \frac{T_{keV}}{511}) \tag{B.5}$$

# C. Properties of 60% hard Oxygen-Free Copper

Copper density is taken as 8940 $kg/m^3$ and not be a function of temperature.

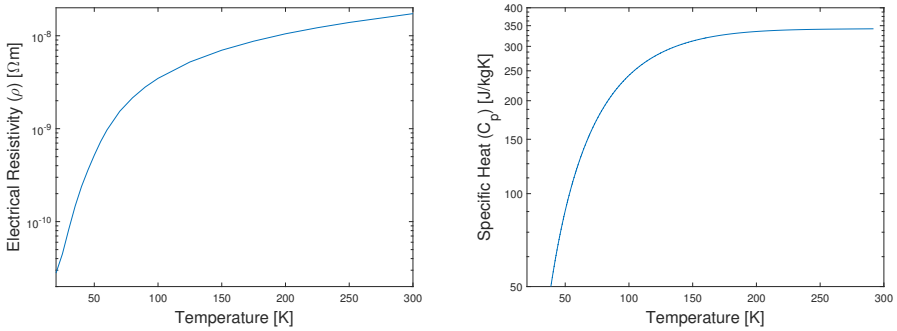


Figure C.1: Left:Copper Resistivity[89], Right: Copper Specific Heat[89]

.

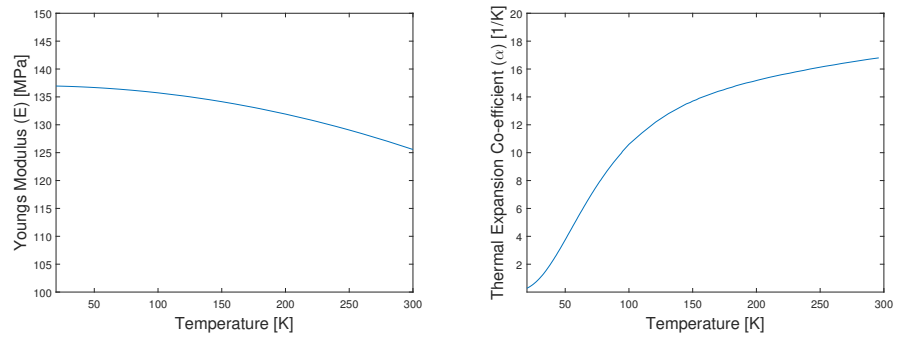


Figure C.2: Left:Copper Young's Modulus[89], Right:Copper Thermal Expansion Co-efficient[89]

.

**Yield Stress** Figure C.4 and the conversion factor (1:0.00689476) from psi to MPa were used to build a table for the yield stress of 60% hard OFCu (aka Copper No. 102).

The rows in (brackets) are calculated using best fit curve from the available data and are of particular interest to LN2 cooled TF coils as 80K is a reasonable starting point for a LN2 cooled coil and 180K is a reasonable end point. Therefore, given a factor of safety of 20% below the yield stress at 180K, the maximum stress allowed at any location in a TF coil is ≈ 250MPa.

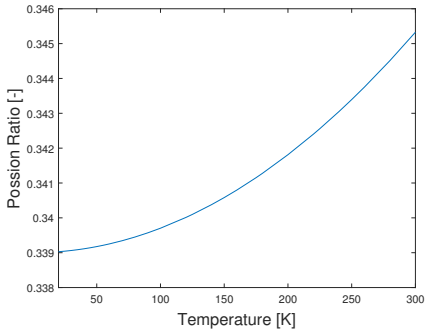


Figure C.3: Copper Poission's Ratio[89]

.

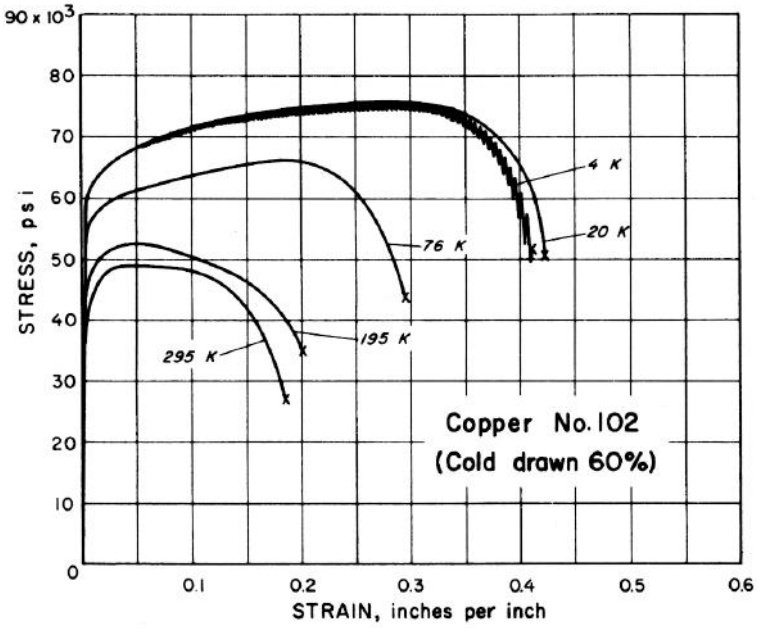


Figure C.4: Copper Stress-Strain Curve for various cryogenic temperaturs[90]

.

| **Temperature** | **Yield Stress** | **Yield Stress** |
|---|---|---|
| [T] | [kpsi] | [MPa] |
| 4 | 58 | 399 |
| 20 | 58 | 399 |
| 76 | 55 | 379 |
| (80) | (54.6) | (376) |
| (180) | (46.3) | (318) |
| 195 | 45 | 310 |
| 295 | 38 | 262 |

Table C.1: Yield Stress of Copper at various cryogenic temperatures. Rows in (brackets) are derived quantities relevant to this investigation.